

*Shashank Ramesh Babu*

THE ONSET OF MARTENSITE  
AND AUTO-TEMPERING IN  
LOW-ALLOY MARTENSITIC  
STEELS

UNIVERSITY OF OULU GRADUATE SCHOOL;  
UNIVERSITY OF OULU,  
FACULTY OF TECHNOLOGY





ACTA UNIVERSITATIS OULUENSIS  
C Technica 775

*SHASHANK RAMESH BABU*

**THE ONSET OF MARTENSITE AND  
AUTO-TEMPERING IN LOW-ALLOY  
MARTENSITIC STEELS**

Academic dissertation to be presented with the assent of the Doctoral Training Committee of Technology and Natural Sciences of the University of Oulu for public defence in the OP-Pohjola auditorium (L6), Linnanmaa, on 5 February 2021, at 12 noon

UNIVERSITY OF OULU, OULU 2021

Copyright © 2021  
Acta Univ. Oul. C 775, 2021

Supervised by  
Professor David Porter

Reviewed by  
Professor Roumen Petrov  
Professor Peter Hedström

Opponents  
Professor Jilt Sietsma  
Professor Peter Hedström

ISBN 978-952-62-2833-4 (Paperback)  
ISBN 978-952-62-2834-1 (PDF)

ISSN 0355-3213 (Printed)  
ISSN 1796-2226 (Online)

Cover Design  
Raimo Ahonen

PUNAMUSTA  
TAMPERE 2021

## **Ramesh Babu, Shashank, The onset of martensite and auto-tempering in low-alloy martensitic steels.**

University of Oulu Graduate School; University of Oulu, Faculty of Technology

*Acta Univ. Oul. C 775, 2021*

University of Oulu, P.O. Box 8000, FI-90014 University of Oulu, Finland

### ***Abstract***

High-strength low-alloy martensitic steels provide low-cost environmentally efficient solutions for weight critical engineering. The wider use of such materials will provide energy savings and reduce the carbon footprint of many products. They offer a combination of both good weldability and high strength, which makes them attractive materials for structural applications. During the rapid transformation, the martensite becomes supersaturated with carbon when compared with the equilibrium ferritic state of the steel. However, when low-carbon steels with high martensitic start temperatures ( $M_s$ ) are quenched, fine carbides can form in the first formed martensite laths. This phenomenon is called auto-tempering. The martensite laths which form at low temperatures remain relatively untempered. Auto-tempered steels exhibit superior toughness and improved formability when compared to steels without auto-tempering. This thesis extends our understanding of auto-tempered martensite in as-quenched low-alloy steels. The tools used were the Gleeble physical simulator for processing the steels, electron microscopy for microstructural characterization, MATLAB to quantify the incidence of carbides in auto-tempered microstructures and Thermo-Calc software to model the microstructure.

Chemical inhomogeneity caused by interdendritic microsegregation is shown to have a major influence on the slow onset of martensite. Combining segregation information with the Koistinen-Marburger equation enabled a good prediction of the experimental martensite evolution curves. The effect of hot mounting during metallographic sample preparation on as-quenched low-alloy steels was investigated. It was found that hot mounting caused additional tempering, which was manifested as new carbides appearing in the regions otherwise free of carbides in auto-tempered microstructures. Electron back scattered diffraction revealed that all the untempered regions in the auto-tempered steel were oriented with  $\{100\}$  planes almost parallel to the broad surface of the hot-rolled steel plate. Martensite orientation variant analysis showed that the auto-tempered and the untempered regions were part of the same packet. A custom-built MATLAB image processing tool was used to quantify the fraction of carbides in auto-tempered microstructures and the frequency distribution of degrees of auto-tempering. The Thermo-Calc modules DICTRA and TC-Prisma were used to compare the precipitation and the partitioning kinetics of carbon during the quenching process. The predictions showed satisfactory agreement with the electron microscopy results, which indicated that the Thermo-Calc software can be used to help design new low-alloy martensitic steels.

*Keywords:* auto-tempering, DICTRA, lath, martensite, quenching, TC-Prisma, Thermo-Calc



# **Ramesh Babu, Shashank, Niukasti seostettujen terästen martensiitin alkulämpötila ja itseispääseminen.**

Oulun yliopiston tutkijakoulu; Oulun yliopisto, Teknillinen tiedekunta

*Acta Univ. Oul. C 775, 2021*

Oulun yliopisto, PL 8000, 90014 Oulun yliopisto

## ***Tiivistelmä***

Suuren lujuusluokan niukasti seostetut martensiittiset teräkset mahdollistavat kustannustehokkaat ja ympäristövaikutuksia huomioivat ratkaisut sovelluksissa, joissa materiaalin massa on ratkaiseva tekijä. Hyvien hitsattavuusominaisuuksien yhdistyminen korkeaan lujuuteen, tekee niistä houkuttelevan vaihtoehdon rakenteellisten sovellusten materiaaliksi. Nopean faasimuutoksen aikana martensiitin hiilipitoisuus ylittää tasapainon mukaisen ferriitin kylläisyysrajan. Korkean martensiitin alkamislämpötilan omaavia vähähiilisiä teräksiä karkaistaessa, hienojakoisia karbideja voi muodostua ensin muodostuneisiin martensiittisäleisiin. Tätä ilmiötä kutsutaan itseispäästöksi. Alhaisemmissa lämpötiloissa muodostuvissa martensiittisäleissä päästö jää suhteellisesti hyvin vähäiseksi. Itseispäästö parantaa sekä lujuutta että muokattavuusominaisuuksia. Tämä väitöskirja laajentaa niukasti seostettujen ja karkaistujen terästen martensiitin itseispäästön tietämystä.

Väitöskirjassa osoitetaan, että kemiallisen koostumuksen epähomogeenisuus, joka johtuu dendriittien välille muodostuvasta mikrosuotaumasta, vaikuttaa huomattavasti martensiitin muodostumisen vaiheittaiseen alkuun. Suotaumasta saadun tiedon yhdistäminen Koistinen-Marburger yhtälöön mahdollisti kokeellisen martensiitin muodostumiskäyrän tarkan ennustamisen. Havaittiin, että kuumenapitus lisää pääsemistä, joka ilmenee uusien karbidien esiintymisenä. Takaisinsironneiden elektronien diffraktion menetelmällä saatu tieto paljasti, että kaikkien niiden alueiden, jotka eivät olleet päässeet, kideaset  $\{100\}$  olivat lähes kohtisuoria kuumavalssatun teräslevyn valssauspintaan nähden. Martensiitin suuntautumisvariantin analyysi osoitti, että itsepäässeet alueet ja ne alueet, joilla päästöä ei ollut tapahtunut, kuuluivat samaan pakettiin. MATLAB ohjelmistolla toteutettua omaa kuvankäsittelytyökalua käyttäen määritettiin karbidien osuus itsepäässeissä mikrorakenteissa sekä itsepääsemisasteen esiintymistiheysjakaumassa. Thermo-Calc ohjelmiston DICTRA ja TC-Prisma osia käytettiin karkaisun aikaisen hiilen erkautumisen- ja jakautumiskinetiikan vertailemiseen. Ennustettu tulos vertautui tyydyttävästi elektroni-mikroskoopilla saatuihin tuloksiin, mikä viittaa siihen että Thermo-Calc voidaan käyttää.

*Asiasanat:* DICTRA, itseispäästö, karkaisu, martensiitti, säle, TC-Prisma, Thermo-Calc



*To my wonderful and supportive family,  
Usha Rani, Ramesh Babu and Harsha Vardhan.*



## Acknowledgements

The research for this thesis towards the PhD was conducted at the Materials and Mechanical Engineering department in the University of Oulu from 2016–2020. This was in cooperation with SSAB Europe Oy, Raahе, Finland. The project was part of the MIMESIS (Mathematics and Materials Science for Steel Production and Manufacturing) project funded by the European Commission grant 675715 – MIMESIS – H2020-MSCA-ITN-2015. This is part of the Marie Skłodowska-Curie Actions within the Horizon 2020 program. I also want to express my gratitude to the University of Oulu Scholarship Fund for awarding me a personal grant. I want to thank SSAB Europe Oy and Outokumpu Oyj for providing the experimental materials which were used for my PhD research.

While I was studying for my Masters at the Ruhr Universität Bochum in Germany in 2012, I came across the book *Phase transformations in metals and alloys*. This turned out to be one of my favourite material science books. I would never have guessed that I would have the opportunity to work towards my PhD with the book's author, Professor David Porter, as my principal supervisor. I still remember vividly when Professor Porter picked me up at the airport when I first arrived in Oulu during the very cold and snowy 2016 February. He has been kind and helpful throughout my stay in Oulu. I have learnt much about approaching research problems and disseminating results. He has been very patient and understanding—listening and answering my innumerable questions. I hope to carry these learnings and develop them wherever I go. I am greatly indebted to him for all his help, support and the knowledge which I gained during my stay in Finland.

I want to thank Dr Pasi Suikkanen from SSAB Europe Oy for all his support during my PhD. I also want to thank Ms Katja Holopainen who has helped me with all the formalities during my employment at SSAB. I also want to acknowledge Dr Saara Mehtonen for helping me get the necessary materials for conducting my experiments. I also want to thank Mr Seppo Ollila, Ms Agne Bogdanoff and Mr Pertti Mikkonen for their help and arrangements during my stay in Raahе. I also want to thank Dr Severi Anttila. He has been very friendly and approachable. His advice has positively contributed to my PhD.

I want to express gratitude to Professor Dietmar Homberg for organising the MIMESIS PhD program at the Weierstrass Institute for Applied Analysis and Stochastics (WIAS), Berlin, Germany. It has been an absolute pleasure to interact with him. I am very grateful for the knowledge he has shared, for the very friendly conversations and for being very approachable. I want to convey my thanks to Dr

Thomas Petzold who was the former MIMESIS program manager. He has dedicated much of his time and energy into organising and making the PhD experience a fruitful one. He was also very friendly during my stay in Berlin. I have to thank both of them for making that experience a great one. I also want to convey my regards to Dr Robert Lasarzik for smoothly taking over the managerial role and his help during the last stages of the PhD program.

I wish to also thank Mr Bjørnar Grande, Mr John-Inge Asperheim and Dr Dmitry “Dima” Ivanov from EFD Induction, Skien, Norway for their support during my stay there. They always checked on me to ensure everything was going smoothly and were very gracious in their welcome. My positive experience of all things Norway can be attributed them. I remember all the interesting conversations and the lunch discussions. I am truly grateful for Dima’s helpful nature and knowledge. I hope to emulate their graciousness when I get to positions similar to theirs in the future.

I want to thank the head of unit, Professor Jukka Kömi, for his important and critical support towards my PhD journey. I want to express my thanks to Dr Mahesh Somani who has always given detailed answers to any question I ask. He has been very helpful and I have learnt a lot about metallurgy from him. I cannot skip thanking the late Mr Seppo Järvenpää. He was very helpful for many things at the university. My PhD would have not gone smoothly without his help. He was also a very friendly and approachable person. I will not forget the impact he had on everyone within our unit. Mr Juha Uusitalo has been very helpful in terms of helping me conduct important tests. He has also been very kind and friendly to me. I express my sincere gratitude to him. Mr Ilpo Alasaarela has also been very helpful in ensuring I get the samples for my work and Mr Tun Tun Nyo has been very cooperative in the sample preparations aspect. I want to thank Mr Jussi Paavola and Dr Olli Nousiainen for their help and cooperation during my PhD research.

I am also thankful to all the colleagues at our unit who have made my stay in Oulu a fruitful one. Dr Aarne Pohjonen is amongst the most knowledgeable people I have met. He is also a very kind and helpful person who can be approached easily. And I also want to thank him for keeping my motorbike safe at his house when I was travelling outside Oulu. It has been a pleasant experience to interact with you. Dr Anna Kisko was also among the people who have been very supportive and friendly during my PhD research. She has always answered my many questions and it is on her advice that I published the paper on the hot mounting effects. I have to express gratitude to Dr Sakari Pallaspuro for his help and especially for his collaboration with one of the papers which contributed to this thesis. He has always

been approachable, friendly and a very good researcher to ideate with. Although he came to Oulu during the latter parts of my PhD period, he made important contributions to this thesis. I want to express my thanks to Mr Jaakko Hannula and Mr Sampo Uusikallio. They have been friendly and helpful during my Oulu period. They have been hospitable and some of my most positive experiences in Finland are because of them. I also want to give my regards to Dr Vahid Javaheri for sharing his help. Dr Mohammed Ali Saleh Fahim was also helpful and I want to convey my thanks to him. And I want to thank for the help from Mr Sami Koskenniska.

I want to express my sincere thanks to the pre-examiners, Professor Roumen Petrov from Ghent University, Belgium, and Professor Peter Hedström from KTH Royal Institute of Technology, Sweden, for taking their valuable time to read and suggest improvements to my thesis.

The PhD journey would not have been fulfilling without the company of good friends. Antti Järvenpää and Matias Jaskari from the Future Manufacturing Technology unit at the University of Oulu have been very important collaborators in my PhD research. They have also been very important in terms of my personal development and have been very encouraging throughout my stay. I cannot thank them enough for their support and also for being great friends. I cannot forget to mention my wonderful friend, Manuel, who has been a constant source of support. I have spent some of my most memorable times with him. I thank him for being there for me throughout my PhD journey. I also want to thank Anna-Lena Kauws, my former classmate and a great friend. She has always been encouraging and supportive. Thank you for being there for me and also for the memorable German Christmas market gift. And of course, I have made many other friends. Henrique, Tom and Prabhjot have been wonderful friends and I have had some of my best conversations with them. Thank you for being there and making life a lot better. And also, Thomas Davis has been a collaborator in my papers and has always been supportive. The summer school in Sweden was one of the highlights of my PhD and it was a great opportunity to meet him there. I want to mention Ms Tiina Ohlsson who organized it and has been a mentor. I want to also thank Ms Tuula Sivonen who was and continues to be my mentor in Oulu. She has given me great advice and has been very approachable. This has positively motivated me, especially during the last stages of the PhD. I want to thank everyone else who I might have missed mentioning here. Thank you for all the good that you have given me.

Last but definitely not the least, I want to thank my family. My parents, Ramesh Babu and Usha Rani, have given me unconditional love and support throughout my

life. My brother, Harsha, has always been there for me. He has given me encouragement throughout my life. They have set me up to be where I am right now. I could not have done it without them being in my life. Thank you for all the sacrifices and love you have given me. I express my sincerest gratitude to you all.

Shashank Ramesh Babu.

Oulu, Finland, November 2020.

## List of abbreviations and symbols

APT	atom probe tomography
CALPHAD	calculation of phase diagrams
EBSD	electron backscatter diffraction
ECD	equivalent circle diameter
EPMA	electron probe microanalyzer
FE-SEM	field emission scanning electron microscopy
FIB	focused ion beam
GDOES	glow discharge optical emission spectroscopy
HAZ	heat affected zone
HV10	Vickers' hardness with a load of 10 kgf
IPF	inverse pole figure
K-M	Koistinen–Marburger
K-S	Kurdjumov–Sachs
NB-SAD	nano-beam selected area diffraction
ND	normal direction
RD	rolling direction
SE	secondary electrons
STEM	scanning transmission electron microscopy
TEM	transmission electron microscopy
TWh	Terawatt-hour
at.%	atom fraction in percent
bcc	body centred cube
bct	body centred tetragonal
$d_c$	correct estimate of the carbide dimension
$d_a$	apparent estimate of the carbide dimension
e.g.	exempli gratia
etc.	et cetera
fcc	face centred cube
i.e.	id est
wt.%	weight fraction in percent
$B$	thermal expansion coefficient in the high temperature limit ( $K^{-1}$ )
$M_s$	martensitic start temperature
$T$	absolute temperature (K)
$T_q$	quench stop temperature

$V_{\alpha}'$	martensite fraction
$D_0^{\alpha}$	theoretical diameter of the sample with a bcc lattice at 0 K
$\Delta D^{\alpha}$	difference in diameter between the ferrite at temperature $T$ and austenite at 0 K
$D_0^{\gamma}$	theoretical diameter of the sample with a fcc lattice at 0 K
$\Delta D^{\gamma}$	change in diameter for austenite due to thermal expansion above 0 K
$D_s$	change in diameter of the specimen due to transformation to martensite
$\alpha$	ferrite
$\alpha'$	martensite
$\beta$	material constant
$\gamma$	austenite
$\Theta_D$	Debye temperature (K)
$\mu$	mean
$\sigma$	standard deviation

## List of original publications

This thesis is based on the following publications, which are referred to throughout the text by their Roman numerals:

- I Ramesh Babu, S., Ivanov, D., & Porter, D. (2019). Influence of microsegregation on the onset of the martensitic transformation. *ISIJ International*, 59(1), 169–175.
- II Ramesh Babu, S., Jaskari, M., Järvenpää, A., & Porter, D. (2019). The effect of hot-mounting on the microstructure of an as-quenched auto-tempered low-carbon martensitic steel. *Metals*, 9(5), 550.
- III Ramesh Babu, S., Nyyssönen, T., Jaskari, M., Järvenpää, A., Davis, T. P., Pallaspuro, S., Kömi, J., & Porter, D. (2019). Observations on the relationship between crystal orientation and the level of auto-tempering in an as-quenched martensitic steel. *Metals*, 9(12), 1255.
- IV Ramesh Babu, S., Davis, T. P., Haas, T., Jarvenpää, A., Kömi, J., & Porter, D. (2020). Image processing tool quantifying auto-tempered carbides in as-quenched low carbon martensitic steels. *Metals*, 10(2), 171.
- V Ramesh Babu, S., Jaskari, M., Jarvenpää, A., Davis, T. P., Kömi, J., & Porter, D. (2020). Precipitation versus partitioning kinetics during the quenching of low-carbon martensitic steels. *Metals*, 10(7), 850.

The author has been the main and corresponding author in all the listed publications. He prepared the research plan, conducted the literature survey, performed the experiments, performed the numerical simulations and compiled the papers. Professor David Porter was the supervisor for the thesis and has also given valuable comments on all the articles. The roles of co-authors in the above manuscripts are as follows:

Dimitry Ivanov derived the closed-form martensite evolution equation and provided the related text in Paper I. Matias Jaskari supported with the FIB milling sample preparation and indexed the TEM diffraction spots in Papers II and V. He also coordinated and processed the EBSD images in Paper IV. Antti Järvenpää reviewed and commented on Papers II, III, IV and V. Tuomo Nyyssönen provided the MATLAB script and provided the related text regarding indexing the martensite variants for Paper III. Thomas Paul Davis reviewed and commented on Papers III, IV and V. Sakari Pallaspuro reviewed and commented on Paper III. Jukka Kömi supported with funding and equipment for Papers III, IV and V. Tim Haas improved the accuracy of the image processing algorithm in Paper IV.



# Contents

<b>Abstract</b>	
<b>Tiivistelmä</b>	
<b>Acknowledgements</b>	<b>9</b>
<b>List of abbreviations and symbols</b>	<b>13</b>
<b>List of original publications</b>	<b>15</b>
<b>Contents</b>	<b>17</b>
<b>1 Introduction</b>	<b>19</b>
1.1 Auto-tempering .....	22
1.2 Gaps in current knowledge and aims of the research .....	24
1.2.1 The slow start of martensite .....	24
1.2.2 Effect of hot mounting on low alloy martensitic steels .....	25
1.2.3 Martensite crystallography .....	25
1.2.4 Quantification of auto-tempering .....	26
1.2.5 Modelling auto-tempering during the quench of low-alloy martensitic steels .....	26
<b>2 Materials and methods</b>	<b>27</b>
2.1 Materials .....	27
2.2 Material processing .....	27
2.3 Material characterization.....	30
2.4 Modelling .....	31
2.5 Image processing.....	36
<b>3 Results</b>	<b>39</b>
3.1 Determination of $M_s$ temperature for the 12Cr steel .....	39
3.2 Effect of hot mounting on the microstructure of the quenched 0.12C low-alloy steel .....	44
3.3 Morphologies of martensite in the quenched 0.12C low-alloy steel .....	47
3.4 Orientations of the auto-tempered martensitic regions .....	48
3.5 Quantification of auto-tempering in the quenched 0.12C low- alloy steel .....	55
3.6 Modelling precipitation and partitioning during quenching.....	57
<b>4 Discussion</b>	<b>65</b>
4.1 Influence of microsegregation on the onset of martensite formation.....	65
4.2 Tempering during hot mounting.....	67

4.3	Relationship between crystal orientation and auto-tempering .....	68
4.4	Image processing toolbox .....	70
4.5	Kinetics of auto-tempering and auto-partitioning during quenching .....	73
<b>5</b>	<b>Summary and conclusions</b>	<b>83</b>
5.1	Influence of microsegregation on the gradual onset of martensitic transformation .....	83
5.2	Effects of hot mounting on the microstructure of as-quenched low-alloy martensitic steels .....	84
5.3	Crystal orientations of the last formed martensitic regions in as- quenched low-alloy martensitic steels.....	84
5.4	Image processing tool to quantify carbides in auto-tempered as- quenched low-alloy martensitic steels.....	85
5.5	Comparison of precipitation and partitioning kinetics occurring during quenching of low-alloy martensitic steels.....	85
<b>6</b>	<b>Novel features</b>	<b>87</b>
<b>7</b>	<b>Future research</b>	<b>89</b>
	<b>List of references</b>	<b>91</b>
	<b>Original publications</b>	<b>97</b>

# 1 Introduction

Iron-based alloys have been and continue to be a critical material for human development. So much so that the third human historical period is called the Iron Age. Therefore, the usage of iron by humans for tool-making covers at least seven millennia (Durand-Charre, 2004). With limited knowledge, early ironsmiths were able to develop their skills and manufactured a range of high-quality products and structures. One famous example is the 7 m wrought-iron pillar in Delhi, India, from the late fourth century (Hosford, 2012). This pillar has been able to resist corrosion for centuries (Hosford, 2012). Iron by itself is a very ductile and malleable material. Therefore, it is commonly alloyed with other chemical elements to make it harder. The alloy of iron and carbon is called steel. Generally, steel contains less than 2 weight percent (wt.%) C while iron with C content above 2 wt.% C is called cast iron (Bramfitt & Benschoter, 2002). Steel is the most successful and cost-efficient in terms of strength per unit price of all metals and continues to be produced in volumes of more than a billion tonnes annually (Bhadeshia & Honeycombe, 2017). The main reason for the dominance of steel is that it can be processed to obtain a huge variety of microstructures and tailored to different properties by various processing routes (Bhadeshia & Honeycombe, 2017).

Today, one of the monumental challenges of the foreseeable future is the reduction of greenhouse emissions, such as carbon dioxide (CO<sub>2</sub>). This can be realized by the usage of efficient materials in weight-critical applications, such as construction and automobiles (Kömi, Karjalainen, & Porter, 2016). Modaresi, Pauliuk, Løvik and Müller (2014) have shown that persistent light-weighting of passenger cars can lead to cumulative greenhouse gas emission savings of 9–18 gigatons CO<sub>2</sub>. A study by the International Transport Forum has shown that reducing the average fleet weight of passenger cars from 1380 kg as recorded in 2015 to 1000 kg by 2050 can result in the reduction of CO<sub>2</sub> emissions by 40% (Elisabeth Windisch, Benezech, Chen, & Kauppila, 2017). The accommodating metallurgy of steel has allowed the development of high-strength steels, leading to manufacturing thinner sections of structures (Béranger, Henry, & Sanz, 1996). This results in considerable weight savings (Béranger et al., 1996). It has been estimated that for every million tonnes of conventional steel that is replaced by advanced high-strength steel in European road cars, there is a life-time saving of 8 million tonnes of CO<sub>2</sub> emissions and 30 TWh of non-renewable energy recourses (Sperle and Hallberg, 2011). Due to their low cost and good weldability, low-carbon (< 0.3 wt.% C) high-strength steels are favoured and are also the focus of the thesis.

It is important to understand the phase transformations and microstructure in steel as they determine its final properties. The phases of steel are ferrite, austenite and cementite. Ferrite ( $\alpha$ -iron) has a body centred cubic (bcc) structure and is stable below 910 °C for pure-Fe. Above this temperature, the crystal structure exists as the face centred cubic (fcc) austenite ( $\gamma$ -iron) in pure-Fe. Carbon is sufficiently smaller in size when compared to iron atoms, thus acting as interstitial solute atoms in the Fe matrix (Bhadeshia & Honeycombe, 2017). Carbon occupies the octahedral interstices in iron. The solubility of carbon is much higher in  $\gamma$ -iron (as high as about 2 wt.%) than in  $\alpha$ -iron (up to a maximum of about 0.02 wt.%) (Bhadeshia & Honeycombe, 2017). This is because of the larger interstices available in  $\gamma$ -iron. Cementite is an iron carbide ( $\text{Fe}_3\text{C}$ ) which generally occurs as precipitates in ferrite. Cementite contains 6.67 wt.% C.

When steel is slowly cooled from high temperatures where austenite is stable, the atoms slowly rearrange to form as ferrite. As the carbon has very low solubility in ferrite, the carbon diffuses out of ferrite and helps in the formation of metastable cementite (graphite is the stable phase when the cooling is extremely slow). But when the cooling rate is sufficiently high, depending on the composition, the crystal structure changes by the simultaneous and cooperative movement of atoms over distances less than the atomic diameter (Pereloma & Edmonds, 2012). The resulting transformed phase is called martensite. This also leads to a change in shape of the transformed region due to the shear and volume expansion (Bhadeshia & Honeycombe, 2017). The shape change caused by martensitic transformation is its most important and defining feature (Pereloma & Edmonds, 2012). The transformation speed of martensite plates is very high (close to 1100  $\text{ms}^{-1}$ ) (Pereloma & Edmonds, 2012). Martensite is also considered to be a metastable phase. Martensite in low-carbon steels containing more than 0.2 wt.% C has a body centred tetragonal (bct) structure while below 0.2 wt.% C it is bcc (Speich & Leslie, 1972). The transformed martensite contributes to a high hardness in steels which are quenched above the critical cooling rate. Therefore, the technological importance of martensite is critical for the development of high-strength steels.

The temperature at which austenite transforms to martensite is called the martensitic start temperature ( $M_s$ ). The alloying elements in the steel have a strong influence on  $M_s$ . Interstitial alloying elements such as C and most substitutional alloying elements suppress  $M_s$ . The substitutional elements, Al and Co, raise  $M_s$  (Durand-Charre, 2004). C has the strongest influence on  $M_s$ . The volume fraction of martensite is dependent on the undercooling below  $M_s$ . The martensite transformation is not thermally activated and takes place independent of time. This

reaction is considered to be athermal (Bhadeshia & Honeycombe, 2017). But it has been documented that martensite can also form isothermally, i.e. with a time dependence, in highly alloyed steels that transform to martensite at sub-zero Celsius temperatures (Villa & Somers, 2020). For plain-carbon steel, the athermal transformation from austenite to martensite has been well described by the Koistinen–Marburger (K-M) equation (Koistinen & Marburger, 1959)

$$V_{\alpha'} = 1 - \exp\{\beta(M_s - T_q)\}, \quad (1)$$

where  $T_q$  is the quench stop temperature below  $M_s$ ,  $\beta$  is a material constant and  $V_{\alpha'}$  is the fraction of martensite.

Due to the coordinated rearrangement of atoms accompanying the phase transformation from austenite (parent phase) to martensite (product phase), there exists a strong crystallographic orientation relationship between the parent and the product lattices. The approximate relationship between parent and the product lattices in low-carbon steels follow the Kurdjumov-Sachs (K-S) orientation relationship and is as follows:  $\{111\}_{\gamma} \parallel \{011\}_{\alpha}$ ,  $\langle 101 \rangle_{\gamma} \parallel \langle 111 \rangle_{\alpha}$ . There are 24 unique K-S orientation relationships between the parent austenite and the product martensite phase (Krauss, 1990; Krauss, 2002; Morito et al., 2003; Hidalgo & Santofimia, 2016). In low-carbon steels, the morphology of martensite is lath-like, as seen in Figure 1. The morphology generally consists of coarse and fine laths in low-carbon steels (Morsdorf, Tasan, Ponge, & Raabe 2015). The morphology is such that the prior austenite grain can be subdivided into packets. The 24 K-S variants can be grouped into four packets. Each packet can be sub-divided into three distinct blocks (Krauss, 1990; Krauss, 2002; Morito et al., 2003; Hidalgo & Santofimia, 2016). The packets and blocks have high angle boundaries ( $> 15^\circ$ ) (Apple, Caron, & Krauss, 1974; Kelly, Jostsons, & Blake, 1990; Huang, Morito, Hansen, & Maki, 2012). In low-carbon low-alloy steels, blocks can be further subdivided into sub-blocks containing pairs of K-S variants with a misorientation of about  $10^\circ$  (Morito et al., 2003). The sub-blocks contain thin parallel laths, which are misoriented by about  $3^\circ$  and made up of the same K-S variant (Morsdorf, 2018).

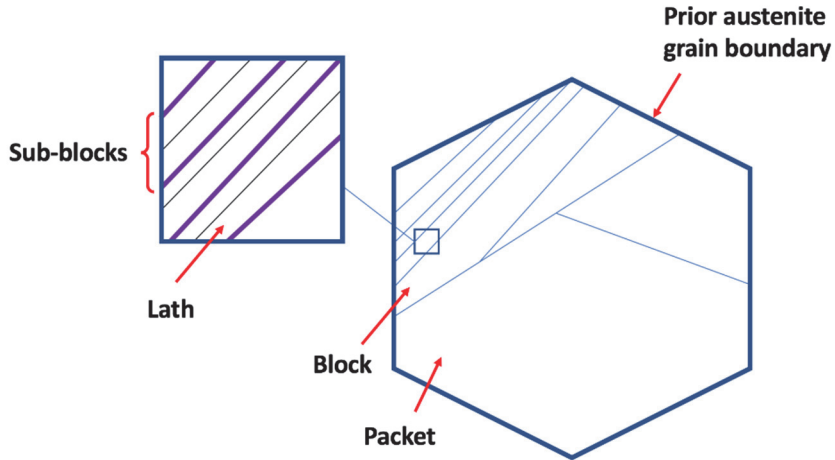


Fig. 1. Schematic of the lath-martensite morphology found in as-quenched steels.

## 1.1 Auto-tempering

As carbon has the strongest tendency of all the alloying elements in depressing the  $M_s$  temperature (Wang, Wolk, & Zwaag, 2000), low-carbon steels have a relatively high  $M_s$  (Pereloma & Edmonds, 2012). When low-carbon steels are quenched below  $M_s$ , the carbon gets redistributed from the super-saturated martensite matrix to form carbides (Bhadeshia & Honeycombe, 2017; Morsdorf, 2018). This phenomenon is called auto-tempering. The difference in chemical potential drives carbon from the interstitial matrix site to the vicinity of a dislocation or grain boundary. The radial diffusion distance for C in ferrite is about 670 nm when cooling from 450 °C to room temperature at a rate of 1000 °C/s and the mean dislocation spacing is about 54 nm when the dislocation density in lath martensite is  $10^{15} \text{ m}^{-2}$  (Morito, Nishikawa, & Maki, 2003). Therefore, it is very reasonable to consider that carbon can diffuse to dislocations especially in laths which form at high temperatures just under  $M_s$  in the case of low-carbon steel, which can also be seen in the atom probe tomography (APT) studies by Hutchinson et al. (2011). Morsdorf et al. (2015) pointed out that the coarse lath regions are the most auto-tempered regions as they are the first to have formed after cooling below  $M_s$ , thereby giving the greatest carbon diffusion distances. Morsdorf et al. (2015) also showed that the carbon almost completely segregates to dislocations and lath boundaries. Carbon diffusion distances are larger for lower cooling rates,

considering that the diffusion distance is inversely proportional to the square root of the cooling rate. Carbon can also diffuse at room temperatures (a carbon atom in ferrite can move a distance of about 96 nm in the radial direction in a week at room temperature when diffusion coefficient =  $2 \times 10^{-6}$  m<sup>2</sup>/s and activation energy = 84098 J/mol (Wert, 1950)). This is not significant due to the low carbon concentrations in the material considered for the thesis.

Auto-tempering in martensite has been shown to have implications for the mechanical properties of the steel. Nam, Yu, and Lee (2019) explored how cold-rollability can be improved by adjusting coiling conditions in the hot-rolling process for medium-Mn steel. It was found that the partial auto-tempering in an air-cooled and coiling simulated specimen resulted in a critical rolling condition of ~68% for cracking when compared to water quenched specimens, for which it was ~30%. The air-coiled and coiling simulated specimens had lower- and wider-ranging hardness values due to the partial auto-tempering occurring after coiling when compared to the water quenched specimens.

Matsuda et al. (2013) studied the effects of alloying elements on the mechanical properties of ferrite-martensite dual phase ultra-high-strength steel with a focus on martensite transformation and the accompanying auto-tempering phenomenon during cooling. When compared to the steel with a higher C content, the Cr and / or B added steel samples had a higher  $M_s$ . The high  $M_s$  in such steels promoted auto-tempering, which resulted in the decrease in difference of hardness between ferrite and martensite. Therefore, this resulted in improved formability of the martensite. They also showed that the well auto-tempered Cr and/or B added steel exhibited higher ductility than carbon-hardened steel (which had a lower  $M_s$ ) when increasing tensile strength over 1500 MPa. With steels having tensile strengths over 1500 MPa, the well auto-tempered Cr and B added steel exhibited higher ductility than the carbon-added steel which contains hard martensite.

Li, Yuan, Ji, Ren, and Wang (2016) studied the behaviour of auto-tempering in rolled plain C-Mn dual phase steels. They showed that when the steel was coiled at 260 °C, auto-tempering softened the martensite. This led to a reduction in the hardness difference between the martensite and ferrite. Due to this, the tensile strength and strain hardening ability decreased and the post-necking elongation increased. The Charpy impact test showed that the auto-tempered steel had a higher toughness when compared to the non-tempered steel. During the tensile test, the ferrite grains and auto-tempered martensite islands elongated as fibrous structures, thereby postponing tensile fracture. This structure might have delayed the formation of micro-voids and crack propagation, thereby delaying tensile fracture

in tensile tests. In impact tests, the fibrous structure might have also inhibited the main crack propagation but induced the branching cracks leading to higher impact energy.

Das, Bhaduri, Srinivasan, Shankar, and Mathew (2009) showed that auto-tempering of the martensitic heat affected zone (HAZ) caused from buttering of 403 martensitic stainless steel with ERNiCr-3 filler material resulted in good bend ductility and high impact toughness of the HAZ. This negates the requirement of any post weld heat treatment which could have caused embrittlement of the weld metal.

Therefore, investigating the auto-tempering phenomenon in as-quenched steels can help in steel composition and processing design for improved property combinations.

## **1.2 Gaps in current knowledge and aims of the research**

### **1.2.1 The slow start of martensite**

The accurate determination of  $M_s$  temperatures is important for making exact predictions of the austenite to martensite transformation below  $M_s$ . This finds application in the development of quenched and partitioned steels where the amount of austenite remaining at the quench stop temperatures is an important factor (Clarke et al., 2008; De Moor, Speer, Matlock, Kwak, & Lee, 2011; Thomas, Danoix, Speer, Thompson, & Cuvilly, 2014).  $M_s$  can be determined using dilatometry, where the volume change which accompanies the fcc to bcc or bct transformation is measured. The K-M equation predicts a sharp discontinuous slope change away from the thermal contraction of the austenite in the length-temperature curve. However, experimentally it is found that the slope change at the onset of martensite is gradual (Yang & Bhadeshia, 2007; Van Bohemen & Sietsma, 2009; Sourmail & Smanio, 2013; Kamyabi-Gol, Clark, Gibbs, Sridhar, & Mendez, 2016). Therefore, techniques such as the offset method have been proposed to define the  $M_s$  in a standard way (Yang & Bhadeshia, 2007). There are also kinetic models which have been formulated to capture the sigmoidal shape of the martensite evolution curve and which better predict the experimental data (Lee & Van Tyne, 2012; Peng, Xu, Han, & Gu, 2019). The possible origins of the gradual onset of martensite (also referred to as “slow-start”) were suggested to be solute segregation during solidification, austenite grain size variation and temperature

gradients (Sourmail & Smanio, 2013). However, these three origins could only explain a minor part of the slow-start phenomenon (Sourmail & Smanio, 2013).

### **1.2.2 Effect of hot mounting on low alloy martensitic steels**

Scanning electron microscopy is often used to characterize carbides in auto-tempered microstructures of as-quenched low alloy martensitic steels as they are not visible using light optical microscopes. Sample preparation involves cutting the specimen at the area of interest, followed by grinding and polishing to remove the deformed layer and to obtain a mirror-like finish, and finally etching with a suitable reagent to reveal the microstructure. The samples are usually mounted in a polymeric resin before the grinding and polishing stage. During the grinding and polishing, this helps to maintain a flat surface, which allows for easy microscopy scanning without the need to change the focus. The sample can either be hot- or cold-mounted. Hot mounting involves thermosetting a specimen in resin under a thermal and pressure cycle in a mounting press. Cold mounting is done by setting the sample in castable resin at room temperature. Hot mounting can be performed within a few minutes while cold mounting usually takes about 24 hours for the curing process. Therefore, hot mounting finds application in a production laboratory where short mounting times are advantageous. It is known that hot mounting can cause visible tempering effects in high-carbon steel (1 wt.% C). However, the effect of hot mounting has not been investigated on as-quenched low-alloy martensitic steels, perhaps because carbon is expected to have either precipitated as carbides or diffused into inter-lath regions due to auto-tempering during quenching.

### **1.2.3 Martensite crystallography**

Austenite grain refinement has been shown to accelerate the martensite transformation during the onset of transformation (Celada-Casero, Sietsma, & Santofimia, 2019). It has also been shown that the volume fraction of the retained austenite is increased when the grain size is reduced (Hidalgo & Santofimia, 2016). The toughness properties of lath martensite are affected by the cleavage crack length, which is determined by the coherence length on the  $\{100\}$  planes approximately perpendicular to the principal stress (Mohrbacher, 2018). Considering these aspects, it is of interest to study the crystal orientations of the

different regions within the lath martensite microstructure and how they vary with respect to the grain size.

#### **1.2.4 Quantification of auto-tempering**

Image processing tools are utilized in metallographic studies to provide quick qualitative and quantitative microstructural analyses. The fractions of carbides in auto-tempered martensite are too small to be detected by physical instruments such as dilatometers. Therefore, an image processing methodology would find application to analyse the carbides in scanning electron micrographs.

#### **1.2.5 Modelling auto-tempering during the quench of low-alloy martensitic steels**

In the production of low-carbon martensitic steels, optimization of cooling strategies and efficient online prediction of steel properties can be achieved by a better understanding of the kinetics and thermodynamics driving the auto-tempering process. The model of auto-tempering developed by Takaki, Akama, and Tsuchiyama (2017) predicts that auto-tempering occurs within the temperature range of 500 °C to 350 °C, but only if the cooling rate is less than 40 °C/s. However, it has been shown that auto-tempering also occurs at rates exceeding 100 °C/s (Paper II). Therefore, there is a need to predict the kinetics of precipitation and partitioning during the quenching of low-carbon steels.

The aims of the current work are to help closing the above gaps in current understanding by addressing the following questions:

- What causes the gradual onset during the martensite transformation and determines the precise value of  $M_s$ ?
- How do the metallographic sample preparation steps affect the auto-tempered microstructure in as-quenched low-carbon steels?
- What are the typical morphologies and orientations of the last formed and first formed martensitic regions?
- How can the volume fraction of auto-tempered precipitates be characterized?
- How can auto-tempering be quantitatively modelled?

## 2 Materials and methods

### 2.1 Materials

The materials used for the thesis were advanced high strength steels that were heat treated to achieve a martensitic microstructure. Paper I investigated the role of microsegregation on the onset of martensite transformation and the determination of the  $M_s$ . This involved study of the dilatation slope changes due to martensite transformation. This necessitated a fully martensitic microstructure. The steel selected was a 12Cr martensitic stainless steel, which was selected due to its high hardenability. This steel was supplied as an 8 mm thick hot-rolled strip made from a continuously cast slab with a thickness of 167 mm. Low-carbon martensitic steels with a relatively high  $M_s$  (380 °C to 440 °C) were also selected so as to have a high degree of auto-tempering. The steels were supplied in the form of 12 mm thick hot-rolled plate.

The chemical compositions of the steels can be seen in Table 1. The mean bulk compositions were determined using glow discharge optical emission spectroscopy (GDOES, Spectruma GDA 750 Analyser). The substitutional alloying element compositions designated by an asterisk (\*) for the martensitic stainless steel used in Paper I were determined using an electron probe micro analyser (EPMA, Jeol JXA-8200 with a LaB<sub>6</sub> filament).

**Table 1. The mean chemical alloying compositions of the studied steels (wt.%).**

Code	Paper(s)	C	Si	Mn	Cr	Ni	Ti	V	Al	Fe
12Cr	I	0.044	0.308*	1.078*	12.117*	0.395*	x	x	x	balance
0.12C	II, III, IV, V	0.126	0.72	1.66	0.27	0.038	0.027	0.047	0.054	balance
0.23C	V	0.223	0.74	1.26	0.25	0.044	0.019	0.043	0.058	balance

### 2.2 Material processing

The martensitic stainless steel for Paper I was cut into cylindrical specimens (∅6 x 36 mm) from the sheet so that the cylinder axes were parallel to the rolling direction. These were thermally processed in a Gleeble 3800 thermomechanical simulator to generate dilatation data. Dilatometry allows for real time monitoring of the phase transformation by measuring the dimensional changes in the sample during a thermal cycle (García de Andrés, 2002). The change in dimensions is due to differences in the specific volumes of the different steel phases (Catteau, Sourmail,

& Moine, 2016). Therefore, it is used extensively to study steel phase transformations (García de Andrés, 2002; Zhao, Mesplont, & De Cooman, 2002; Oliveira, Andrade, & Cota, 2007).

The samples were heated by resistive electric heating through the cylinder from copper sliding jaws that held the specimen, as seen in Figure 2. Type K thermocouples spot-welded to the surface of the specimen at the mid-length were used to record the temperatures. Specimens were heated at the rate of 10 °C/s from room temperature to 1050 °C, held at this temperature for two minutes and then cooled back to room temperature at the rate of 48 °C/s. In the Gleeble, cooling is by heat flow into the copper jaws, which are themselves bolted into water-cooled aluminium jaw carriers.

The samples for Papers II, IV and V were cut into  $\varnothing 6 \times 9$  mm cylinders with their long axes along the principal rolling direction of the hot-rolled plate. They were then processed in the Gleeble between copper anvils with a heating rate of 10 °C/s to 950 °C, holding for two minutes to ensure austenitization, and finally quenching into a beaker of water placed below the anvils. Type K thermocouples spot-welded to the mid-length of the cylinder surfaces recorded a quench rate of 2000° C/s. By using the ELTA electromagnetic and thermal calculation software (Bukanin, Zenkov, & Ivanov, 2016), it was estimated that the cooling rate at the centre of the specimen would be 1000° C/s. For Paper IV, another set of samples was cooled by the aluminium jaw carriers at a rate of 100 °C /s and for Paper V at a rate of 120 °C /s. The cooling rates considered in the study were determined so as to ensure a fully auto-tempered martensitic microstructure. This was after experimental verifications which showed the presence of bainite even for cooling rates of 60 °C/s.

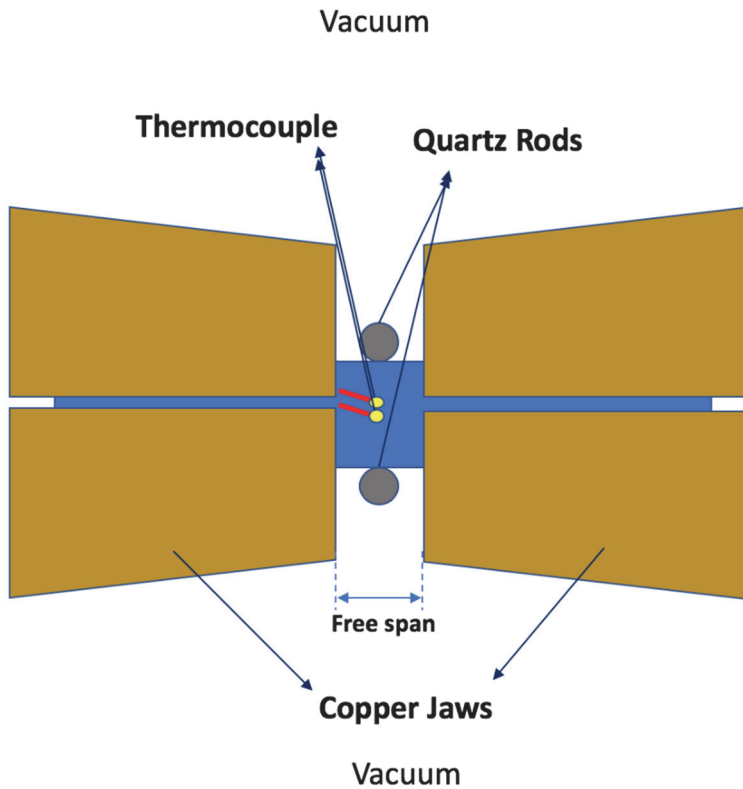


**Fig. 2. Schematic of the cylindrical steel specimen held by copper jaws on a Gleeble 3800 thermomechanical simulator. The quartz rods are located across the diameter of the sample. Free span is 6 mm for a cylinder length of 36 mm (Modified from Paper I).**

For Paper III, samples with the dimensions of 20 x 10 x 10 mm were cut from the hot-rolled plate with their long side parallel to the rolling direction. There were austenitized at 917 °C in an inert argon gas atmosphere in a Nabertherm L5/11 furnace for 24 hours to produce a bimodal prior austenite grain size distribution. The samples were then quenched in water to obtain a fully martensitic microstructure.

## 2.3 Material characterization

After cutting from regions of interest, the microscopy samples were ground and polished to remove the deformed layer. The final polishing procedure was made with a force of 10 N and at a speed of 150 rpm for five minutes using a 40 nm colloidal silica suspension to achieve a mirror-like surface finish. The samples were then etched in a solution comprising 2% HNO<sub>3</sub> in ethanol (2% Nital) for 10 s to reveal the microstructure. Before the grinding and polishing stages, samples are usually mounted in a polymeric resin which helps maintain a flat surface (Bramfitt & Benschoter, 2001). This flat surface allows for easy scanning without changing the focus when viewed under a light optical microscope (Bramfitt & Benschoter, 2001). The mounting materials can be classified as hot mounts and cold mounts. Hot mounting is performed under a temperature and pressure cycle in a mounting press using thermosetting resins. Cold mounts are made by curable cast mounting material at room temperature. It is known that hot mounting causes tempering effects in the case of high-carbon steels containing about 1 wt.% C (Bramfitt & Benschoter, 2002). The possible effects of hot mounting in the case of low-carbon steels were studied in Paper II by using both hot and cold mounting. Further details are given in Paper II. The EPMA line measurements used for Paper I were made on transverse sections of the specimens which were cut and polished at the thermocouple location.

Conventional light microscopy cannot resolve carbides in auto-tempered microstructures due to their small dimensions. Therefore, field emission scanning electron microscopy (FE-SEM) (Zeiss Sigma at 5 kV with an aperture diameter of 30 µm) was used in Papers II, III, IV and V.

Crystal orientations were determined using electron backscattered diffraction (EBSD) on another SEM (Zeiss Ultra Plus at 15kV with an aperture size of 120 µm, minimum step size of 0.03 µm) equipped with an EBSD detector (Oxford Instruments). EBSD was used in Papers I and III. The EBSD samples were prepared in a similar way to the FESEM samples but without being etched in Nital. The AztecHKL software from Oxford instruments was used to process the EBSD maps. HKL Channel 5 Tango software was used to conduct noise-reduction to fill in non-indexed patterns in EBSD maps. The noise reduction process used six neighbouring points and resulted in less than 10% modification of the indexed points. The bulk compositions were determined using the electron probe microanalyzer (EPMA) (Jeol JXA-8200 with a LaB<sub>6</sub> filament). For Papers I and III, prior austenite grain size was determined using the austenite reconstruction algorithm given by

Nyyssönen, Peura, and Kuokkala (2018). The algorithm was built using the MTEX texture analysis MATLAB toolbox (Bachmann, Hielscher, & Schaeben, 2010). The martensite variant analysis and the misorientation angle calculations were also made using the same toolbox in Paper III.

Transmission electron microscopy (TEM) and scanning transmission electron microscopy (STEM) (JEOL 2200FS STEM/TEM) were utilized to acquire high resolution images of the carbides in auto-tempered microstructures.

TEM samples were prepared using focused ion beam (FEI Helios DualBeam) milling of the processed steel samples as described in Papers II and V. Nano-beam selected area diffraction patterns (NB-SAD) were used to identify precipitates.

## 2.4 Modelling

The use of thermodynamic and kinetic calculation tools has been seen to be a powerful way of understanding phase transformations (Andersson, Helander, Höglund, Shi, & Sundman, 2002). To this end, Thermo-Calc, DICTRA and TC-Prisma have been used in this thesis. Thermo-Calc (Sundman, Jansson, & Andersson, 1985) is a thermodynamic CALPHAD (Calculation of Phase Diagrams) approach (Lukas, Fries, & Sundman, 2007), which can be used to make all kinds of phase transformation, phase diagram and thermodynamic assessments (Andersson et al., 2002). CALPHAD involves the calculation of thermodynamic quantities and simulation of phase transformations from free energy as a function of temperature, composition and pressure (Lukas et al., 2007). The approach involves obtaining mathematical expressions for the free energy using statistical mechanics models. Then the free energy function is fitted to the selected thermodynamic information by parameter adjustment. These parameters are then compiled into a database (Kaufman & Ågren, 2014).

DICTRA is a software tool used to simulate diffusion controlled transformations (Andersson, Höglund, Jönsson, & Ågren, 1990; Borgenstam, Höglund, Ågren, & Engström, 2000) and is built to handle multi-component alloying systems. The simulations are performed by utilizing simple 1-D geometries (planar, cylindrical or spherical). The basis of DICTRA is multicomponent diffusion theory, which describes the flux of species driven by concentration gradients (Borgenstam et al., 2000) and is also detailed in Paper V. The diffusion equations are solved by coupled partial differential equations which are extended to multicomponent systems. The DICTRA simulations require thermodynamic and kinetic databases. The kinetic databases were calculated using

CALPHAD methodology wherein the atomic mobility of individual species in a multicomponent phase is a function of temperature, composition and pressure (Borgenstam et al., 2000). Storing individual mobilities rather than interdiffusion coefficients in the database is more efficient as there are  $n$  mobilities but  $(n-1)^2$  interdiffusion coefficients in an  $n$  component system (Borgenstam et al., 2000). Therefore, this allows for efficient use of storage space (Borgenstam et al., 2000). As the accuracy of the DICTRA simulations is dependent on the accuracy of the databases and assumptions such as those used for geometries, they have been compared with experimental data for validation (Borgenstam et al., 2000).

TC-Prisma is a Thermo-Calc module which can be used to simulate precipitation kinetics for a variety of growth mechanisms and thermal histories (Chen, Wu, Sterner, & Mason, 2014). The module is based on the Langer–Schwartz theory (Langer & Schwartz, 1980) and adopts the Kampmann–Wagner numerical method (Wagner, Kampmann, & Voorhees, 2005) for simulating the nucleation, growth and coarsening of precipitate phases. TC-Prisma extends classical nucleation theory to multi-component systems (Thermo-Calc Software AB, 2019) and is also described in Paper V. TC-Prisma can also be applied to real systems by the usage of appropriate thermodynamic and kinetic databases. The most important parameter for the precipitation calculations is the interfacial energy, but it is a difficult parameter to obtain experimentally (Chen et al., 2014). Therefore, it is important to choose an approximate value to start the calculations and then find an appropriate value which best fits the experimental data.

As Thermo-Calc and its accompanying modules are not exact simulation tools, appropriate geometries and approximations have to be made.

In Paper I, DICTRA was used to obtain the carbon concentration profile in austenite under the influence of the substitutional alloying elements after two minutes at 1050 °C considering the microsegregation of substitutional alloying elements. Therefore, a planar geometry of length 1 mm was set up which was discretized to 100 equidistant points. With austenite as the phase, the carbon profile was initialized as a uniform distribution. The concentration of substitutional alloying elements along the 1 mm line was experimentally determined using EPMA.

In Paper II, DICTRA was used to explore the potential growth of cementite precipitating in the martensite matrix during the hot mounting of metallographic specimens. The precipitates were assumed to nucleate with zero incubation time as soon as the martensite lath has formed. In that way, it was possible to analyse the precipitation using the DICTRA diffusion software. Simulations were made considering a binary Fe-C system to avoid the convergence errors that are

encountered with multicomponent systems at high cooling rates. This should not lead to significant errors as the early cementite growth stage is expected to occur without appreciable substitutional diffusion (Hou, Hedström, Xu, Di, & Odqvist, 2014; Klein, Mujica Roncery, Walter, Weber, & Theisen, 2017). The closed cylindrical cell shown in Figure 3 was used as the simulation set-up. The distance between two cementite precipitates was approximately 100 nm as per the TEM observations, which will be detailed in the results section. Therefore, initially, a 50 nm radius ferrite matrix cell was assumed with the cementite set to grow from its centre as a rod-shaped precipitate. Bcc ferrite had to be chosen to represent the martensite in the DICTRA diffusion calculations. This is probably a reasonable approximation as far as lattice diffusion is concerned, as low-carbon lath martensite is expected to lose its tetragonality by disordering (Zener, 1946). The disordering is due to the carbon atom jumping from an octahedral site, which would cause the tetragonality in the c-axis, to an adjacent site, thereby obtaining the bcc ferrite structure. There would be around eight dislocations within the 50 nm cylinder radius when the dislocation density is  $10^{15} \text{ m}^{-2}$ . However, these dislocations would be aligned parallel to the central dislocation on which the precipitate grows in the 1-D DICTRA model. Therefore, the dislocations would not be supplying carbon to the precipitate by the pipe diffusion mechanism. Instead, they would release their carbon into the matrix in favour of the growing precipitate. Therefore, the cementite radius is expected to increase mainly by lattice diffusion to the precipitate without much assistance from pipe diffusion. Due to the limitations of the DICTRA software, capillary effects were ignored. The predicted initial growth rate would be reduced if capillary effects would have been included. Therefore, the calculated radius is an upper bound.

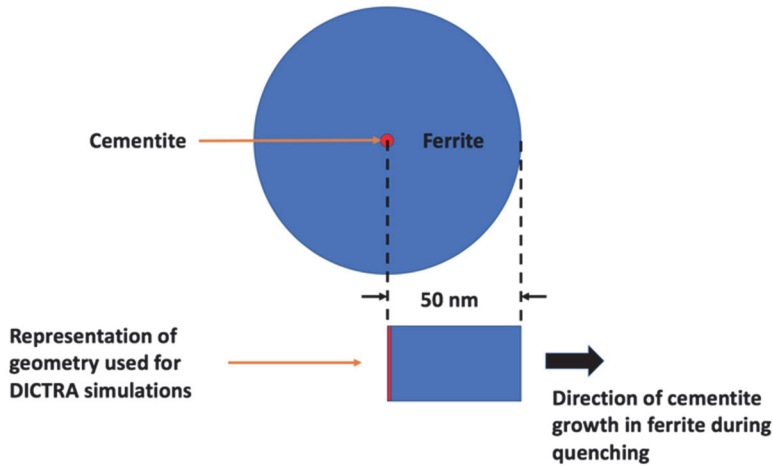


**Fig. 3. Schematic of the simulation set-up used in DICTRA with a 0.1 nm radius cementite located at the centre of a 50nm radius ferrite cylinder (Reprinted under CC-BY 4.0 license from Paper II © 2019 Authors).**

In Paper IV, Thermo-Calc was used to predict the equilibrium fraction of cementite at room temperature.

In Paper V, DICTRA was used to simulate the diffusion of carbon from martensite into the retained austenite during auto-tempering and TC-Prisma was used to simulate the carbon depletion from the martensite matrix during precipitation of cementite during auto-tempering. The main assumption for the calculations is that these processes are assumed to be independent alternatives as opposed to the real situation wherein they are competing processes. The geometry for the DICTRA simulations is shown in Figure 4. It was assumed that the carbon content was uniform immediately after the formation of the lath. The ferrite and the attached austenite phases were considered as coupled cells with an immobile interface and equal carbon activities in the two phases at the interface (Hillert, Höglund, & Ågren, 1993; Borgenstam et al., 2000). The STEM results in Paper V showed that the coarse martensitic regions had thicknesses greater than 1000 nm while the smallest lath thickness was about 100 nm. Therefore, as seen in Figure 4, the DICTRA geometries were set up so that the laths forming close to  $M_s$  had a half-thickness of 500 nm and the laths forming after 90% of martensite had formed was set to a half-thickness of 50 nm. Concentration profiles were calculated at six

locations, i.e. 0, 25, 50, 75, 90 and 100% of the half-thickness, as shown in Figure 4.

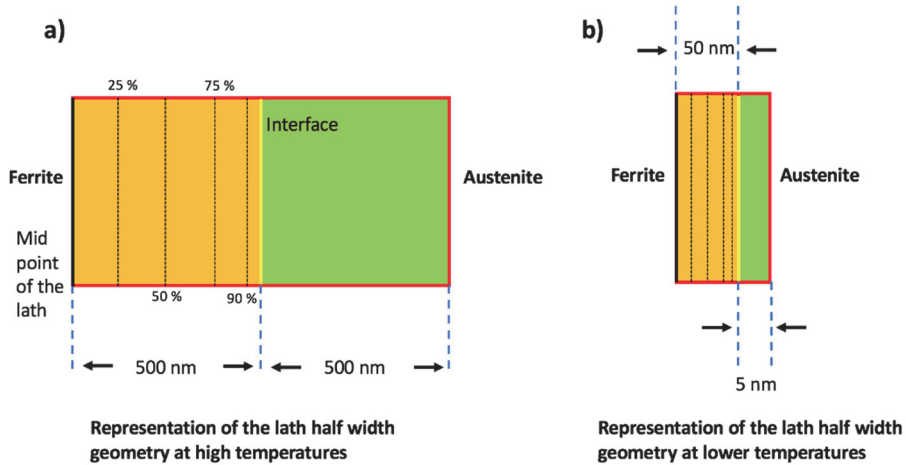


**Fig. 4. Schematic of the geometry used in the DICTRA simulations showing assumed ferrite and austenite half-thicknesses, where a) represents the situation just under the  $M_s$  temperature and b) represents the situation when approximately 90% of the austenite has transformed to martensite. The black, yellow and the dotted lines within the geometry are the locations where the change in carbon concentration was calculated (Reprinted under CC-BY 4.0 license from Paper V © 2020 Authors).**

TC-Prisma also considered a disordered bcc martensite in which the precipitation of cementite is modelled assuming that the carbides are nucleated on dislocations and that no carbon is lost via diffusion to the surrounding austenite. On the basis of measurements made by Morito, Nishikawa, and Maki (2003) on low-carbon steels, the dislocation density in ferrite was taken as  $10^{15} \text{ m}^{-2}$ .

The assumed formation temperatures of the coarse and fine laths are given in Table 2. Both the diffusion and precipitation simulations were run for cooling rates of  $1000 \text{ }^\circ\text{C/s}$  and  $120 \text{ }^\circ\text{C/s}$ .

**Table 2. Start temperatures for the diffusion and precipitation simulations in Paper V (Reprinted [adapted] under CC-BY 4.0 license from Paper V © 2020 Authors).**

Steel Code	500 nm ferrite half-thickness	50 nm ferrite half-thickness
	Lath formation temperature (°C)	Lath formation temperature (°C)
0.12C	435	300
0.23C	388	290

## 2.5 Image processing

A custom-built image processing program to quantify the auto-tempered precipitates in electron micrographs was made using MATLAB. The methodology involves the selection of a SEM micrograph from the region of interest, as shown in the schematic Figure 5a. This image is then binarized into a black and white image, as shown in Figure 5b. An appropriate threshold feature pixel count is applied to discriminate and remove the longer grain and lath boundary features from the image, as shown in Figure 5c. The resultant image comprises features containing fewer pixels than the threshold value, as seen in Figure 5d. This image contains the precipitates and other features. Due to the limitations of the image resolution, the resulting image consists of features which represent the precipitates and some grain boundary portions which were not extracted as continuous boundary features. A second stage of the image analysis process therefore involves the calculation of the ratios of the major and minor axes of all the features. Then the features which have a ratio larger than a specified threshold are deleted, thereby providing an image with only the features representing the precipitates. This image was then further processed by dividing it into a matrix of equisized 100 pixel by 100 pixel boxes. The ratio of white pixels to the total pixels within each box is then calculated. Depending on the ratio, the box regions are designated a colour which indicates the degree of local area auto-tempered carbide fractions (see Figure 6). Yellow represents the boxes in which the apparent auto-tempered precipitate area fraction exceeds 10%. The green boxes are those in which the apparent local auto-tempered precipitate area fraction ranges from 1–10%. The blue boxes indicate area fractions of less than 1%. The methodology will be demonstrated on an SEM micrograph in the results section.

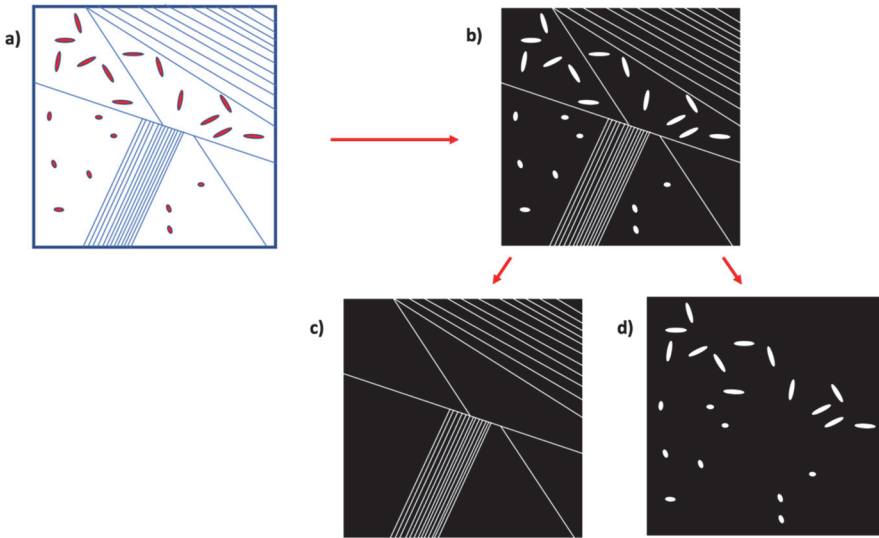


**Fig. 5. Schematic of the MATLAB image processing program routine which isolates precipitates in scanning electron micrographs of auto-tempered martensite (Reprinted under CC-BY 4.0 license from Paper IV © 2020 Authors).**

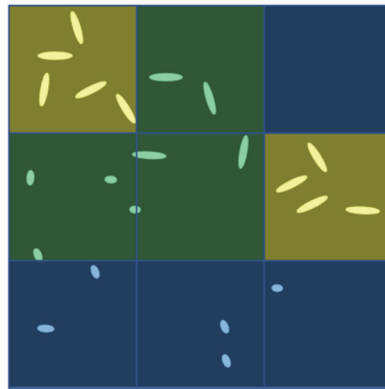


**Fig. 6. Schematic of the image-processed micrograph showing coloured equisized squares. The colours indicate the degree of auto-tempering wherein the apparent local area fraction of carbides in auto-tempered microstructures decreases from yellow through green to blue (Reprinted under CC-BY 4.0 license from Paper IV © 2020 Authors).**



### 3 Results

#### 3.1 Determination of $M_s$ temperature for the 12Cr steel

The examples of elemental distributions from the 12Cr steel (Paper I) as measured with the EPMA and its histogram representation of the same for Cr and Mn can be seen in Figure 7. The mean and the standard deviations for the measured elemental data can be seen in Table 3. The accuracy of the EPMA results was determined by measuring from standard samples with the same measurement parameters as those which were used for the 12Cr steel specimen. The standard deviations for measured intensities between the standard sample and the 12Cr steel specimen were all below 0.25 %. The carbon profile was calculated using DICTRA as it is problematic to accurately measure carbon content with the EPMA due to hydrocarbon contamination on the sample surface (Yamashita, Tanaka, Nagoshi, & Ishida, 2016). The resulting profile was one where carbon diffuses into the regions with high concentrations of Mn and Cr. This is because Mn and Cr lower the activity of carbon.

**Table 3. Overall means and standard deviations of elemental concentrations (wt.%) (Reprinted [adapted], with permission, from Paper I © 2019 ISIJ).**

Value	Cr	Mn	Si	Ni	C
mean	12.117	1.078	0.308	0.395	0.0440
Std.dev.	0.541	0.046	0.025	0.044	0.0017

Cr, Mn, Si and Ni measured using the EPMA. C was measured using GDOES Analyzer

The  $M_s$  temperature is assumed to be linearly related to the alloying chemical compositions and is determined using the equation

$$M_s = a_0 + a_C C + a_{Mn} Mn + a_{Si} Si + a_{Cr} Cr + a_{Ni} Ni + a_{Mo} Mo + a_{Co} Co. \quad (2)$$

Here,  $a_0$ ,  $a_C$ ,  $a_{Mn}$ , etc., are experimentally determined coefficients available in the literature and the elemental symbols represent the alloying element concentrations in wt.%. The Kung and Rayment formula (Kung & Rayment, 1982) was found to be best suited for determining the  $M_s$  of the stainless steel sample used in Paper I. The coefficients of the formula can be seen in Table 4.

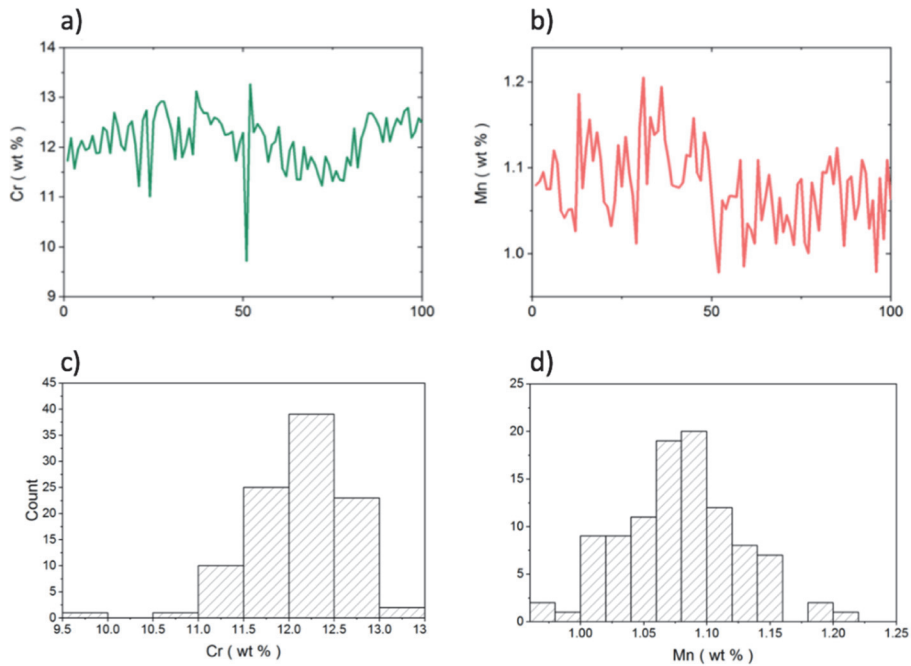


**Fig. 7. Elemental distributions for a) Cr and b) Mn. 100 EPMA values from a line scan of 1 mm in length. Histograms showing variations in the concentrations of Cr (c) and Mn (d) (Reprinted, with permission, from Paper I © 2019 ISIJ).**

The K-M equation is then used to calculate the martensite fraction evolution for each local composition. The start temperatures were determined from Equation 2 using the unmodified coefficients in Table 4. The final martensite fraction is calculated as the sum of the contributions from the 100 local compositions.

**Table 4. Unmodified coefficients of the Kung and Rayment formulae (Reprinted [adapted], with permission, from Paper I © 2019 ISIJ).**

Formula	$a_0$	$a_c$	$a_{Mn}$	$a_{Si}$	$a_{Cr}$	$a_{Ni}$	$a_{Mo}$	$a_{Co}$
Kung and Rayment	539	-423	-30.4	-7.5	-12.1	-17.7	-7.5	+10

The non-linear equations of van Bohemen (2013) for the dilatation of austenite and ferrite as a function of temperature (Equations 3 and 4) were used to construct the dilatation of the specimen through the phase transformation. The equations used are

$$\frac{\Delta D^\gamma}{D_0^\gamma} = B_\gamma + B_\gamma \Theta_D^\gamma \left[ \exp\left(-\frac{T}{\Theta_D^\gamma}\right) - 1 \right] \quad (3)$$

and

$$\frac{\Delta D^\alpha}{D_0^\alpha} = \frac{D_0^\alpha - D_0^\gamma}{D_0^\alpha} + B_\alpha T + B_\alpha \Theta_D^\alpha \left[ \exp\left(-\frac{T}{\Theta_D^\alpha}\right) - 1 \right], \quad (4)$$

where the superscripts and subscripts  $\gamma$  and  $\alpha$  refer to the austenite and ferrite phases, respectively,  $T$  is the absolute temperature,  $\Theta_D$  is the Debye temperature,  $B$  is the thermal expansion coefficient in the high temperature limit,  $\Delta D^\gamma$  is the change in diameter for austenite due to thermal expansion above 0 K,  $D_0^\gamma$  is the theoretical diameter of an austenitic sample at  $T = 0$  K,  $D_0^\alpha$  is the diameter of the sample with a bcc lattice at  $T = 0$  K,  $\Delta D^\alpha$  is the difference in diameter between the ferrite at temperature  $T$  and austenite at 0 K. The coefficients seen in Table 5 were used as they allowed for the best fit with the experimental dilatometry curves.

**Table 5. Coefficients used for the construction of the Bohemen dilatation model (van Bohemen (2013) for austenite and ferrite (Reprinted [adapted], with permission, from Paper I © 2019 ISIJ).**

Phase	$B$ ( $K^{-1}$ )	$\Theta_D$ (K)
Austenite	23.89e-6	274
Ferrite	18.1e-6	335

Using the fraction of martensite calculated from the sum of the contributions from the 100 local compositions ( $f_m$ ), the change in the diameter of the specimen during transformation to martensite is given by the equation

$$D_s = D^\gamma + (D^\gamma - D^\alpha) f_m. \quad (5)$$

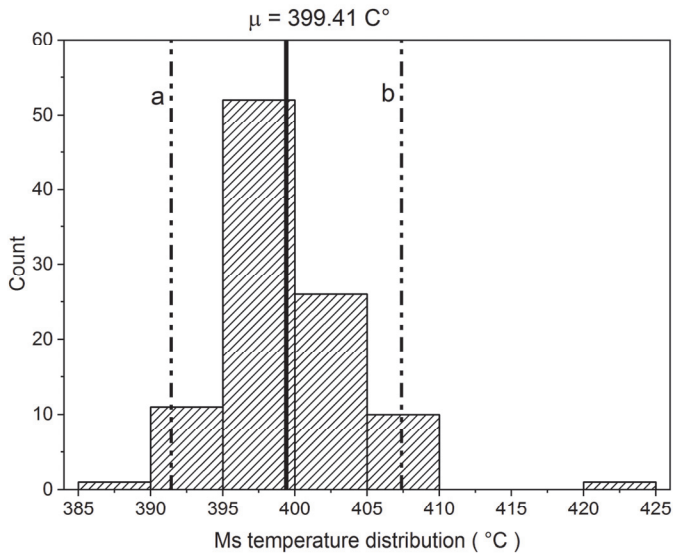
By modifying the coefficients  $a_0$  and  $a_{C\gamma}$  in the Kung and Rayment formula and the material constant  $\beta$  in Equation 1, the sum of squares of the differences between the experimentally measured dilatation curves and the predicted specimen diameter from Equation 5 were minimized (over the temperature range 385 °C to 425 °C). The Kung and Rayment parameters modified for the fit are seen in Table 6. The finalized fit value for  $\beta$  was 0.0159  $K^{-1}$ .

**Table 6. Modified coefficients of the Kung and Rayment formulae (Reprinted [adapted], with permission, from Paper I © 2019 ISIJ).**

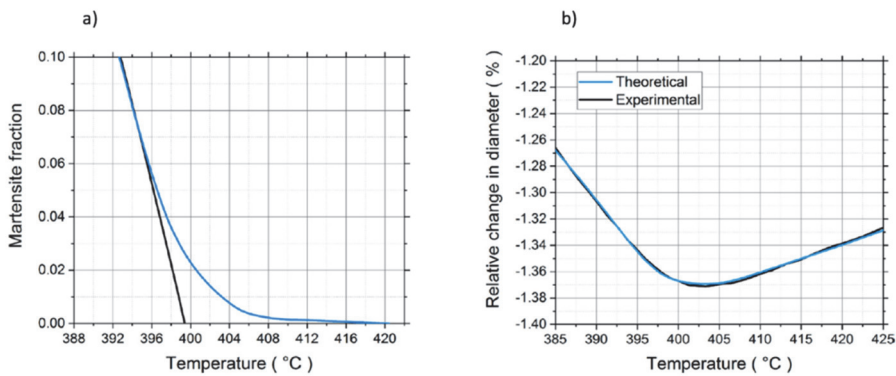
Formula	$a_0$	$a_C$	$a_{Mn}$	$a_{Si}$	$a_{Cr}$	$a_{Ni}$	$a_{Mo}$	$a_{Co}$
Kung and Rayment (modified)	538	-423	-30.4	-7.5	-6.43	-17.7	-7.5	+10

Figure 8 shows the histogram which represents the local  $M_s$  temperature distribution calculated from the local compositions using the modified Kung and Rayment formula.

The resulting gradual onset of martensite fraction evolution calculated from the K-M equation considering the contributions of the 100 analysed points can be seen in Figure 9a. The sharp onset as predicted by the K-M equation considering the mean composition representing a homogeneous specimen can also be seen in Figure 9a. The tail from the gradual martensite onset tends towards higher temperatures than the mean  $M_s$ . The theoretical dilatometric curve as calculated by the methodology stated in the previous paragraphs and corresponding experimental results during the martensite onset can be seen in Figure 9b.



**Fig. 8.** Histogram of the  $M_s$  temperatures as determined by the modified Kung and Rayment empirical formula. The parameters  $a$ ,  $b$  and  $\mu$  are for Equation 6 explained in the Discussion section (Reprinted, with permission, from Paper I © 2019 ISIJ).



**Fig. 9.** a) Martensite volume fraction vs temperature, wherein the blue line is from the sum of the contributions from the 100 measured local compositions and the black line represents the mean composition. b) Comparison between the theoretical and the experimentally determined dilatometry curves at the onset of martensite formation (Reprinted, with permission, from Paper I © 2019 ISIJ).

### 3.2 Effect of hot mounting on the microstructure of the quenched 0.12C low-alloy steel

The effects of mounting were studied using the 0.12C steel specimen which was austenitized and quenched at 1000 °C/s (Paper II). The SEM micrograph in Figure 10 shows the microstructure of the as-quenched auto-tempered martensite steel specimens moulded into the cold (Figure 10a) and hot (Figure 10b) mounts. The carbide precipitates vary from place to place in terms of size and area density in both specimens. The darker regions are those where there are negligible to no precipitates. The distribution of precipitates is denser in the dark regions of the hot-mounted specimens when compared to the cold-mounted specimens.

TEM/STEM was used to resolve the auto-tempered precipitates in the coarse martensite region, as seen in Figures 11a and 11b. The precipitates were rod/plate-like and were identified as cementite using selected area diffraction, as seen in Figure 11c and 11d. Neither epsilon nor Hägg carbides were found.

The hardness values for the hot- and cold-mounted specimens can be seen in Table 7. A standard two-tailed *t*-test using the StatPlus software (Version v6, AnalystSoft, Inc.) was implemented to compare the hardness values. The low *p*-value of 0.039 (< 0.05) shows that with 95% certainty there is a difference between the hardness values of the hot- and cold-mounted specimens, indicating that the hardness increases during hot mounting.

**Table 7. HV10 hardness data from hot- and cold-mounted specimens (Reprinted under CC-BY 4.0 license from Paper II © 2019 Authors).**

Mounting	Hot	Cold
Mean	443.65	432.55
Standard deviation	16.71	16.03
Number of measurements	20	20
Lower 95 % confidence limits for the mean	435.83	425.05
Upper 95 % confidence limits for the mean	451.47	440.05

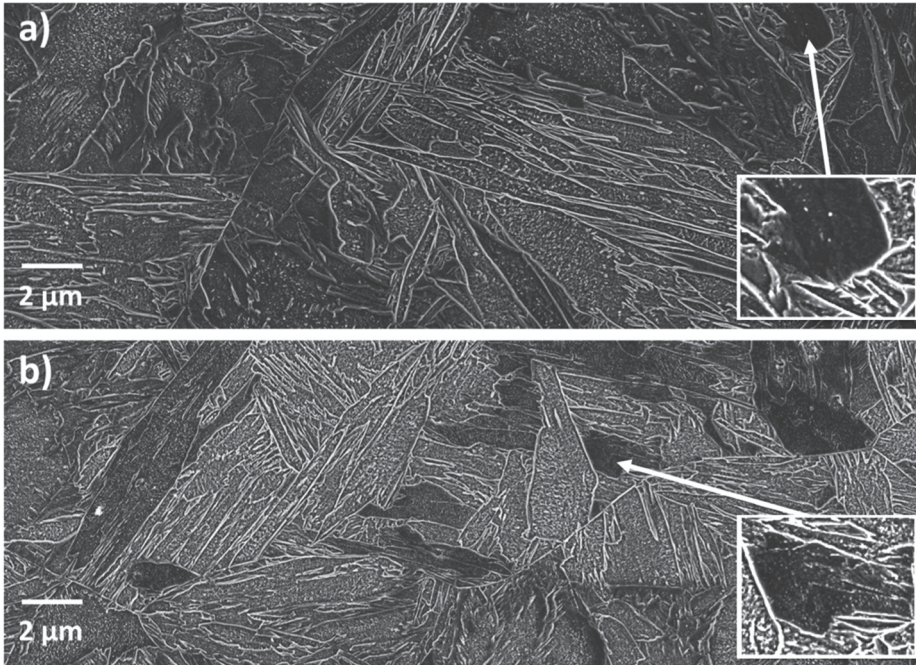


**Fig. 10. Scanning Electron Microscopy (SEM) micrographs from the centres of transverse cross-sections of the 0.12C steel specimens which were austenitized and quenched at 1000 °C/s, where a) cold-mounted and b) hot-mounted. Insets show the magnified images of regions which had the lowest density of auto-tempered precipitates (Reprinted under CC-BY 4.0 license from Paper II © 2019 Authors).**

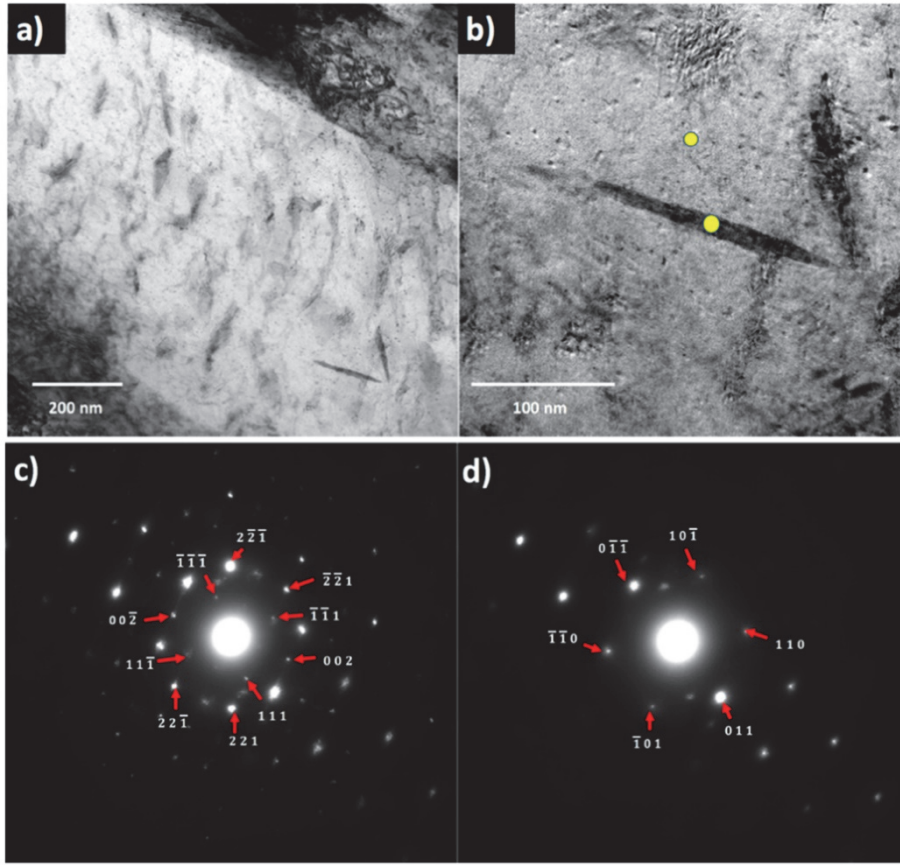
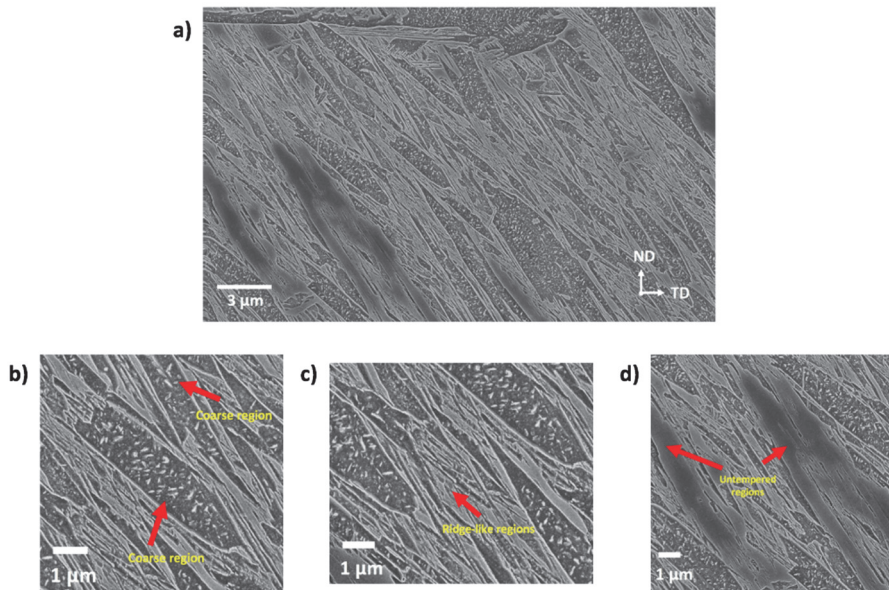


Fig. 11. Transmission and scanning transmission electron microscopy (TEM/STEM) micrographs of the hot-mounted 0.12C steel specimen which was austenitized and quenched at 1000 °C/s. a) STEM image of the coarse martensitic lath with cementite precipitates; b) TEM image of cementite precipitate, with yellow dots denoting the location of nanobeam selected area diffraction (NB-SAD) patterns; c) NB-SAD pattern with indexed cementite diffraction spots, zone axis  $[110]$ ; d) NB-SAD pattern with indexed ferrite matrix spots, zone axis  $[111]$  (Reprinted under CC-BY 4.0 license from Paper II © 2019 Authors).

### 3.3 Morphologies of martensite in the quenched 0.12C low-alloy steel

The 0.12C steel was heat treated for 24 hours at 917 °C to obtain a bimodal distribution of prior austenite grain sizes. The large grains had a diameter of ca. 300  $\mu\text{m}$  and the small grains a diameter of ca. 17  $\mu\text{m}$  (Paper III). After quenching the sample in water, the resultant microstructure comprised of the auto-tempered martensite is as shown in Figure 12.



**Fig. 12.** a) SEM micrograph which shows the auto-tempered lath martensite typical for as-quenched low carbon steels. Indicated by the red arrows are b) coarse auto-tempered martensite regions, c) ridge-like martensitic regions and d) untempered regions (Reprinted [adapted] under CC-BY 4.0 license from Paper III © 2019 Authors).

The morphology was classified into three categories, namely: coarse auto-tempered regions, ridge-like regions and untempered regions.

The coarse regions are wedge-shaped with a high density of auto-tempered precipitates, as seen in Figure 12b. The matrix of the coarse regions is also the most highly etched when compared to the other features of the microstructure.

The ridge-like regions are features which appear as narrow raised bands, as seen in Figure 12c. They form around the coarse auto-tempered features. These

regions consist of clusters of fine martensitic laths which etch to different degrees. The carbides in the ridge-like regions are either absent or smaller than the precipitates found in the coarse auto-tempered regions.

Untempered regions are unetched featureless regions with almost no visible carbides, as seen in Figure 12d. The regions have a plateau-like topography in contrast to the ridge-like and the coarse auto-tempered regions.

### 3.4 Orientations of the auto-tempered martensitic regions

The EBSD inverse pole figure (IPF) map and the corresponding SEM micrograph of a martensitic region within a large grain (Equivalent circle diameter (ECD) = 289  $\mu\text{m}$ ) from the 0.12C steel which was austenitized for 24 hours and quenched, can be seen in Figure 13. The colours indicate the crystallographic orientations of the plate normal, i.e. thickness, direction. The coarse auto-tempered and ridge-like regions are oriented with  $\{111\}$ //ND to  $\{112\}$ //ND, i.e. in the regions of the stereographic triangle coloured light blue to purple. The ridge-like features appear to have formed with the same orientation as that of the adjacent first formed coarse regions. However, throughout the grain, the untempered regions are oriented with  $\{100\}$ //ND, i.e. the red regions of the stereographic triangle. The slightly tempered regions containing small carbides are shaded orange, which corresponds to the  $\{103\}$ //ND. These regions have an island-shaped morphology.

The EBSD IPF map and corresponding SEM micrograph in Figure 14 show the smaller grains (mean ECD = 16.9  $\mu\text{m}$ , standard deviation = 9.4  $\mu\text{m}$ ). Similar to the observations in the large grain, the EBSD IPF red-coloured regions, which have  $\{100\}$ //ND, are untempered. This observation applies to all grains irrespective of the orientations of the neighbouring coarse auto-tempered and ridge-like regions.

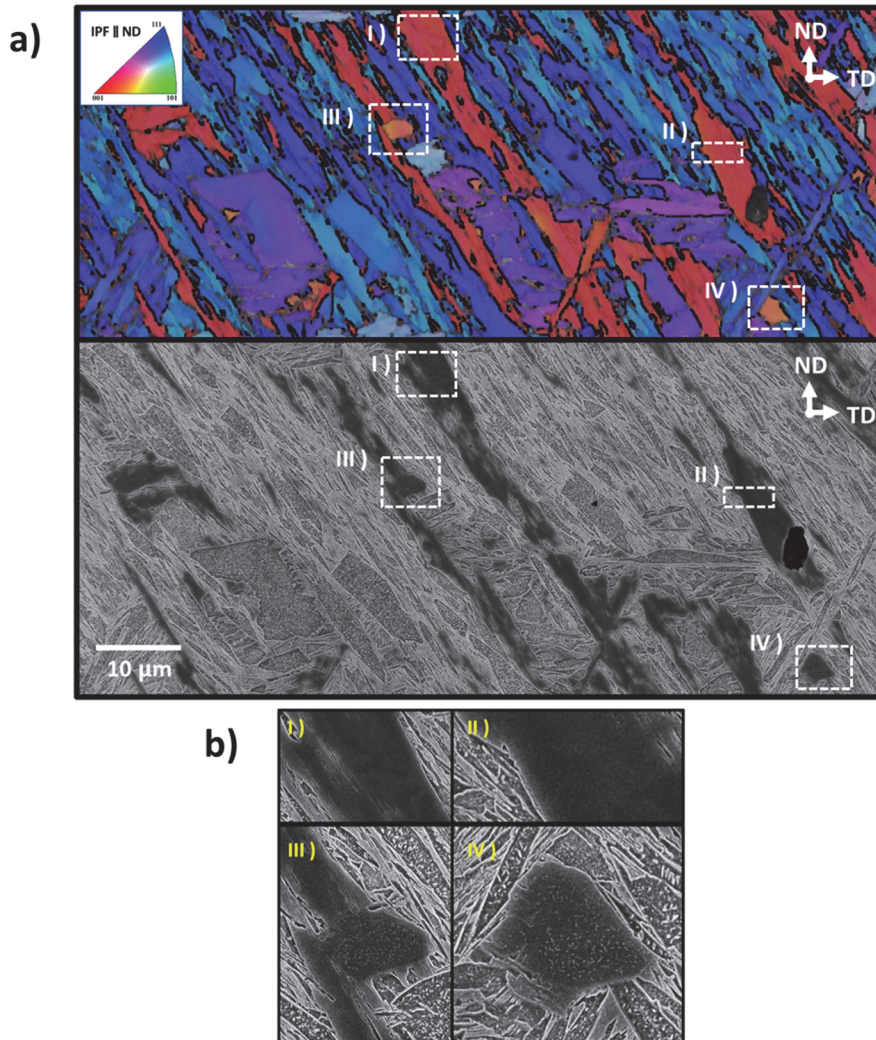


**Fig. 13.** Micrographs from the from the 0.12C steel which was austenitized for 24 hours and quenched, where a) electron backscattered diffraction (EBSD) normal direction (ND) inverse pole figure (IPF) map and the corresponding SEM image inside a large grain (Equivalent circle diameter = 289 μm). The colours represent the crystallographic orientation of the plate normal. b) SEM image of the regions marked (I) and (II) (red shades in the IPF) and regions marked (III) and (IV) (orange shades in the IPF), as seen in a). The red shaded regions are relatively untempered while the orange shaded regions show slight tempering (Reprinted [adapted] under CC-BY 4.0 license from Paper III © 2019 Authors).

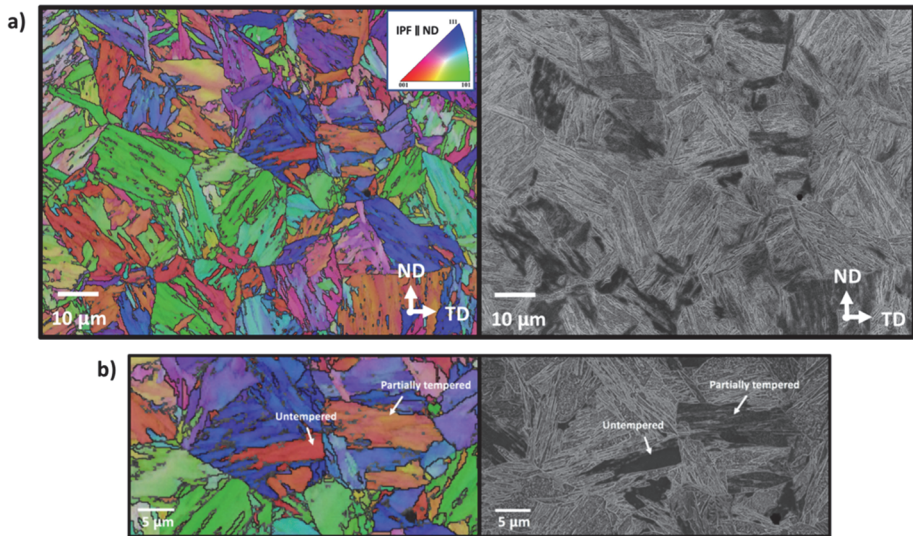


**Fig. 14.** Micrographs from the 0.12C steel which was austenitized for 24 hours and quenched, where a) EBSD ND IPF coloured map and corresponding SEM micrograph of small grains; b) magnified EBSD ND IPF coloured map and corresponding SEM micrograph comparing the IPF red and orange-coloured regions that are tempered and partially tempered, respectively (Reprinted [adapted] under CC-BY 4.0 license from Paper III © 2019 Authors).

Figures 15 and 16 show martensite variant maps and corresponding variant histograms for the two prior austenite grain sizes. The numbers in the figures indicate the different variants within the K-S orientation relationship based on the scheme introduced by Morito et al. (2003). The variants have been grouped based on having same close-packed planes, i.e. V1 to V6, V7 to V12, V13 to V18 and V19 to V24, as described by Morito et al. (2003) and Nyssönen et al. (2018). Each group of variants form as martensite packets. As was shown in low-carbon steels by Morito et al. (2003), the packets are subdivided into blocks containing specific sub-block pairs misoriented by about 10 degrees. For example, the sub-block variant pairs within the V1–V6 packet are V1/V4, V2/V6 and V3/V6.

The misorientation map was segmented using the MTEX software into a grain map using a 3° angular threshold followed by a manual selection of grains which correspond to the untempered regions seen in Figure 13 and Figure 14. The software was used for crystallographic reconstruction of the prior austenite grains after which the relationship of the untempered regions and its neighbouring areas were further examined. The reconstruction algorithm was carried out according to

the methodology proposed by Nyysönen et al. (2018). The mean  $\gamma/\alpha'$  orientation relationship was determined iteratively from intergranular misorientations on the basis of which the variant map was constructed. They are indexed according to Table 8, which shows the 24 martensite variant pairs corresponding to all possible angle-axis pairs. This variant map was overlaid onto an EBSD band contrast map, as seen in Figures 15 and 16. The packets can be identified using the colour scheme, which helps in visual determination of the packet structure.

The large grain, as seen in Figure 15a, predominantly comprises packet V1–V6 (V1/V4, V2/V5 and V3/V6 block variant pairs) and packet V19–V24 (V19/V22, V20/V23 and V21/V24 block variant pairs). The histogram in Figure 15b shows that the variants are distributed evenly in the packet V1–V6 while the block V19/V22 is dominant within the packet V19–V24. The untempered regions, which are outlined by a white line in Figure 15a, belong to the dominant packet, V1–V6, although they might share some of their boundaries with another packet. The untempered regions are almost exclusively made up of the block V2/V5 (approximately 87.6% of the indexed orientation pixels within untempered regions). This was the case even in the untempered regions surrounded by other packets.

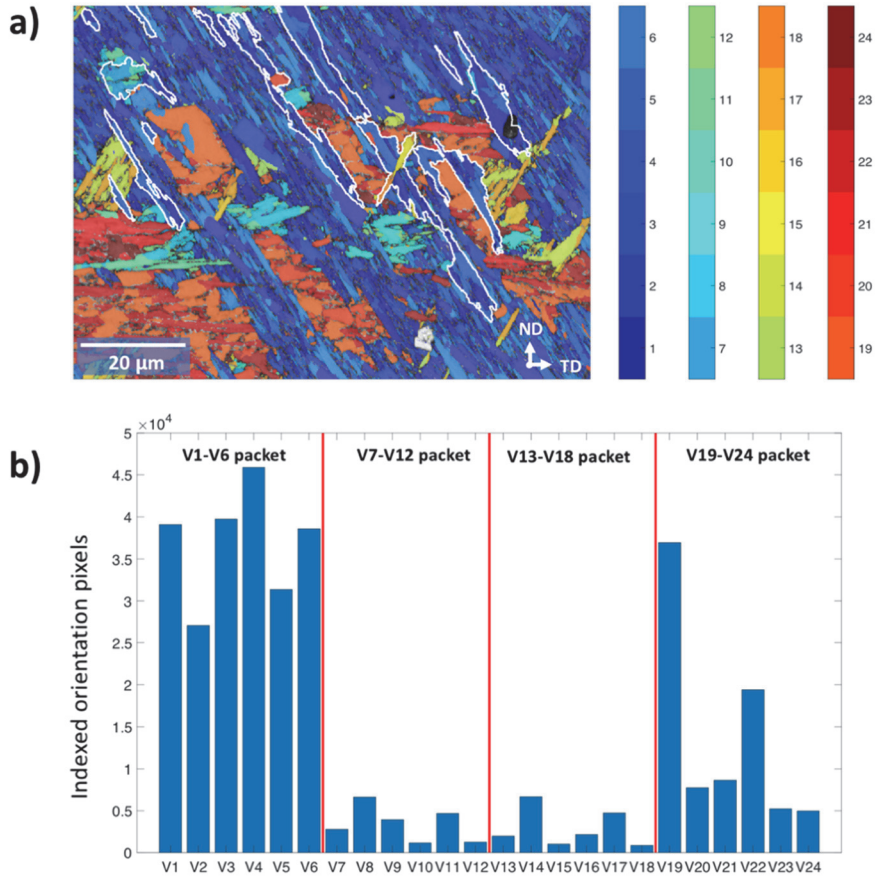


**Fig. 15. a) EBSD band contrast map within a large grain in the 0.12C steel which was austenitized for 24 hours and quenched, with the variant colouring overlaid with the corresponding variant colour key. The variant index follows the scheme described in Table 8. The untempered regions are enclosed by white boundaries. b) Histogram showing the variant distribution in the region covered in a) (Reprinted [adapted] under CC-BY 4.0 license from Paper III © 2019 Authors).**

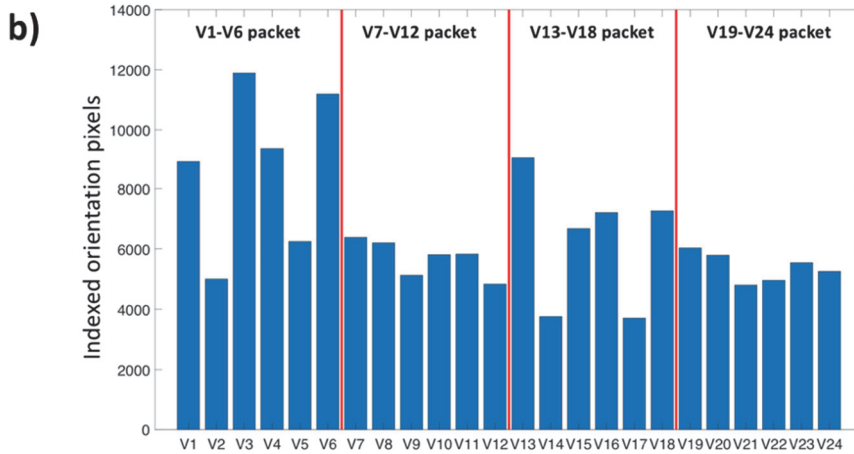
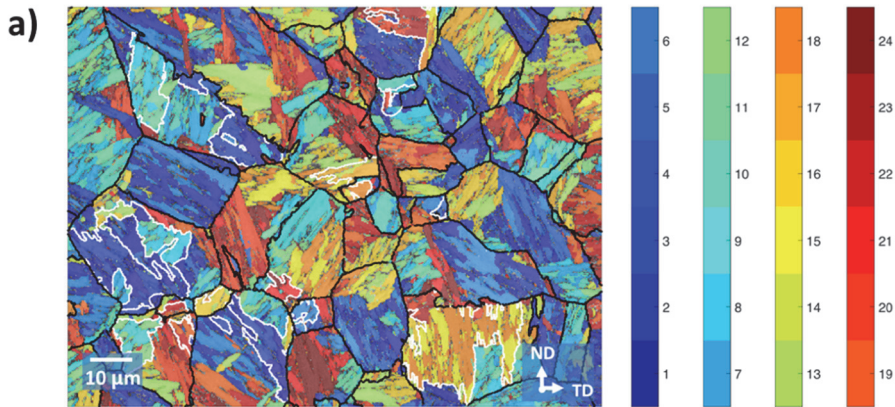


**Fig. 16. a) EBSD band contrast map of small grains in the 0.12C steel which was austenitized for 24 hours and quenched, with the variant colouring overlaid with the corresponding variant colour key. The variant index follows the scheme described in Table 8. The untempered regions are enclosed by white boundaries. b) Histogram shows the variant distribution from the region seen in a) (Reprinted [adapted] under CC-BY 4.0 license from Paper III © 2019 Authors).**

**Table 8. The 24 martensite orientation variants based on the mean representative K-S orientation relationship during the reconstruction procedure described by Morito et al. (2003) (Reprinted [adapted] under CC-BY 4.0 license from Paper III © 2019 Authors).**

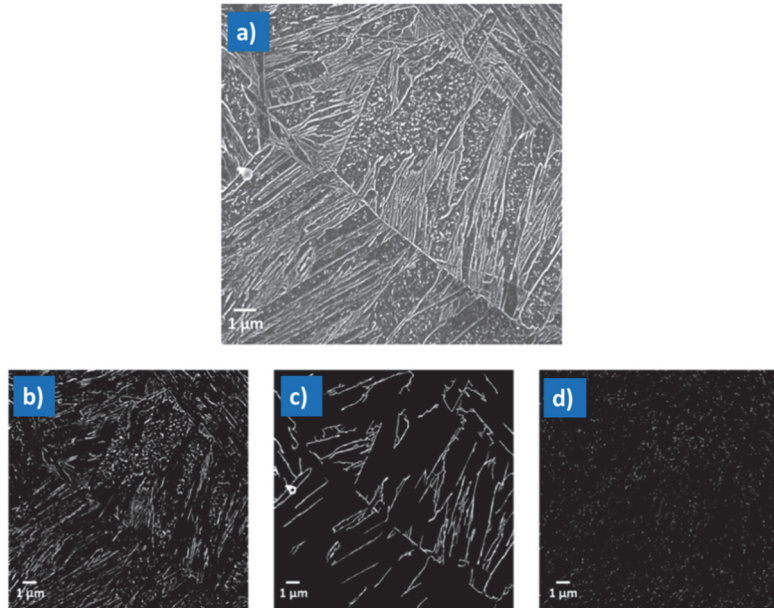
Variant No.	Plane Parallel	Direction Parallel	Rotation from Variant 1			
		$[\gamma] \parallel [\alpha']$	Axis		Angle [deg.]	
V1	(111) $\gamma$ $\parallel$ (011) $\alpha'$	$[\bar{1}01] \parallel [\bar{1}\bar{1}1]$	-			0
V2		$[\bar{1}01] \parallel [\bar{1}\bar{1}\bar{1}]$	-0.5190	0.5459	0.6577	60.2703
V3		$[01\bar{1}] \parallel [\bar{1}\bar{1}1]$	-0.5131	0.4719	0.7170	59.9978
V4		$[01\bar{1}] \parallel [\bar{1}\bar{1}\bar{1}]$	-0.5285	-0.0000	0.8489	4.7482
V5		$[\bar{1}\bar{1}0] \parallel [\bar{1}\bar{1}1]$	-0.4719	0.5131	0.7170	59.9978
V6		$[\bar{1}\bar{1}0] \parallel [\bar{1}\bar{1}\bar{1}]$	-0.7065	0.0408	0.7065	55.4056
V7	$(\bar{1}\bar{1}1)\gamma$ $\parallel$ (011) $\alpha'$	$[\bar{1}0\bar{1}] \parallel [\bar{1}\bar{1}1]$	-0.6098	0.5062	0.6098	51.6135
V8		$[\bar{1}0\bar{1}] \parallel [\bar{1}\bar{1}\bar{1}]$	-0.6979	0.1607	0.6979	9.6813
V9		$[\bar{1}\bar{1}0] \parallel [\bar{1}\bar{1}1]$	-0.6625	0.2135	0.7179	52.7289
V10		$[\bar{1}\bar{1}0] \parallel [\bar{1}\bar{1}\bar{1}]$	-0.4489	0.5800	0.6798	51.3062
V11		$[011] \parallel [\bar{1}\bar{1}1]$	-0.5135	0.0557	0.8563	12.7631
V12		$[011] \parallel [\bar{1}\bar{1}\bar{1}]$	-0.6610	0.1906	0.7258	57.3000
V13	$(\bar{1}\bar{1}1)\gamma$ $\parallel$ (011) $\alpha'$	$[0\bar{1}1] \parallel [\bar{1}\bar{1}1]$	-0.0557	0.5135	0.8563	12.7631
V14		$[0\bar{1}1] \parallel [\bar{1}\bar{1}\bar{1}]$	-0.5800	0.4489	0.6798	51.3062
V15		$[\bar{1}0\bar{1}] \parallel [\bar{1}\bar{1}1]$	-0.2437	0.6713	0.7000	56.4210
V16		$[\bar{1}0\bar{1}] \parallel [\bar{1}\bar{1}\bar{1}]$	-0.6953	0.1819	0.6953	15.5492
V17		$[110] \parallel [\bar{1}\bar{1}1]$	-0.6508	0.3912	0.6508	51.1570
V18		$[110] \parallel [\bar{1}\bar{1}\bar{1}]$	-0.2734	0.6585	0.7011	51.9818
V19	(11 $\bar{1}$ ) $\gamma$ $\parallel$ (011) $\alpha'$	$[\bar{1}\bar{1}0] \parallel [\bar{1}\bar{1}1]$	-0.2135	0.6625	0.7179	52.7289
V20		$[\bar{1}\bar{1}0] \parallel [\bar{1}\bar{1}\bar{1}]$	-0.1906	0.6610	0.7258	57.3000
V21		$[0\bar{1}\bar{1}] \parallel [\bar{1}\bar{1}1]$	-0.1058	0.0000	0.9944	17.6963
V22		$[0\bar{1}\bar{1}] \parallel [\bar{1}\bar{1}\bar{1}]$	-0.6585	0.2734	0.7011	51.9818
V23		$[101] \parallel [\bar{1}\bar{1}1]$	-0.6713	0.2437	0.7000	56.4210
V24		$[101] \parallel [\bar{1}\bar{1}\bar{1}]$	-0.2427	-0.0000	0.9701	18.0592

The variant map of the region of small grains is shown in Figure 16a. The smaller grains consist of correspondingly smaller sized packets. The packets consist of several blocks with the untempered regions constituting a single block. Depending on the grain concerned, the untempered regions comprise the blocks V1/V4, V7/V10, V8/V11, V13/V16, V14/V17 and V20/V23. The histogram in Figure 16b shows that the variants are evenly distributed in the packets V7–V12 and V19–V24. The blocks V1/V4 and V3/V6 dominate the packet V1–V6. The blocks V13/V16 and V15/V18 dominate the packet V13–V18.

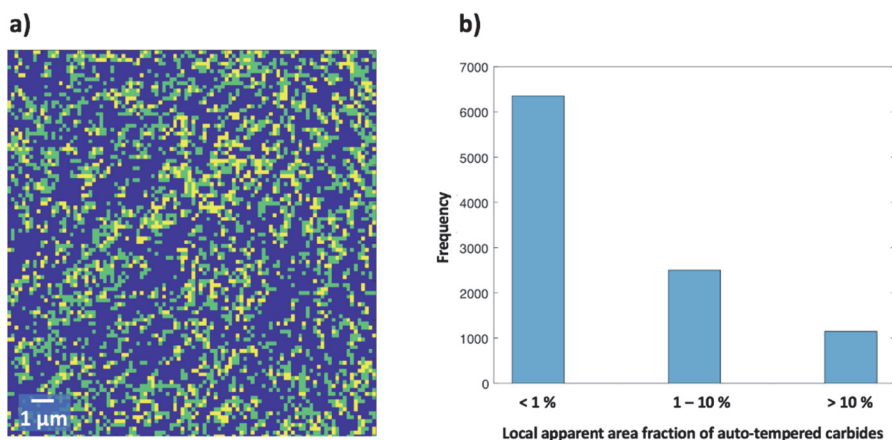
### 3.5 Quantification of auto-tempering in the quenched 0.12C low-alloy steel

Figure 17a shows the SEM micrograph of the 0.12C steel sample quenched at 100 °C/s. This image is grey-scaled and the high-intensity pixels of the image indicate the grain boundaries and the precipitates within the martensitic matrix. As described in the methodology section, this image was binarized, as shown in Figure 17b, so that the non-matrix features are positive (indicated by white pixels) while the background was set to zero (indicated by the black colour). The larger features which indicate the grain and lath boundaries, as seen in Figure 17c, were separated from the smaller precipitate features, as seen in Figure 17d, by using a threshold pixel value (number of pixels  $\geq 30$ ). The area fraction of the auto-tempered precipitates was found to be 3.02% using the custom MATLAB program. This is an overestimation when compared to the equilibrium volume fraction predicted using Thermo-Calc (Andersson et al., 2002), i.e. 1.84% at 23 °C.

Figure 18a shows the corresponding colour map indicating the local area fractions of the carbides in auto-tempered microstructures. The colours indicate the degree of the apparent fractions, where the yellow regions have  $> 10\%$ , green regions have 1–10% and blue regions have  $< 1\%$  area fractions of carbides in auto-tempered microstructures. Figure 18b shows the histogram for the same apparent local area fractions of the carbides in auto-tempered microstructures.



**Fig. 17. a) SEM micrograph of 0.12C steel sample quenched at 100 °C/s; b) binary image of the SEM micrograph, as seen in a); c) segmented binary image with grain boundaries (threshold pixels  $\geq 30$ ); d) segmented binary image of the precipitates (threshold pixels  $< 30$ ) (Reprinted [adapted] under CC-BY 4.0 license from Paper IV © 2020 Authors).**



**Fig. 18. a) Colour map indicating the apparent local area fractions in the sample, where the colours yellow, green and blue represent > 10%, 1–10% and < 1% area fractions of carbides in auto-tempered microstructures, respectively; b) histogram showing the local area fraction distribution of carbides in auto-tempered microstructures (Reprinted [adapted] under CC-BY 4.0 license from Paper IV © 2020 Authors).**

### 3.6 Modelling precipitation and partitioning during quenching

Electron microscopy was used to determine lath dimensions and precipitate identities in the 0.12C and 0.23C steels after austenitizing and quenching at 1000 °C/s and 120 °C/s. Figures 19 and 20 show the microstructures of the 0.12C steel quenched at 1000 °C/s and 120 °C/s, respectively. They reveal a typical auto-tempered lath martensite morphology with dark, untempered regions as the last to form, as described in section 3.3. The apparent thicknesses of the coarse martensite regions ranged from 1 to 5 µm. The STEM images revealed that the apparent thicknesses of the smaller laths were about 100 nm. The precipitates in both the samples were identified as cementite.

Figures 21 and 22 show the microstructures of the 0.23C steel samples quenched at 1000 °C/s and 120 °C/s, respectively. They also reveal the typical auto-tempered lath martensite morphology. But unlike the 0.12C steel, the relatively dark regions showed some signs of auto-tempering. The widths of the coarse martensite regions and the smaller laths were similar to those in the quenched 0.12C steel. Here, too, the precipitates were identified as cementite. There was no evidence of other types of carbides in either steel grade.

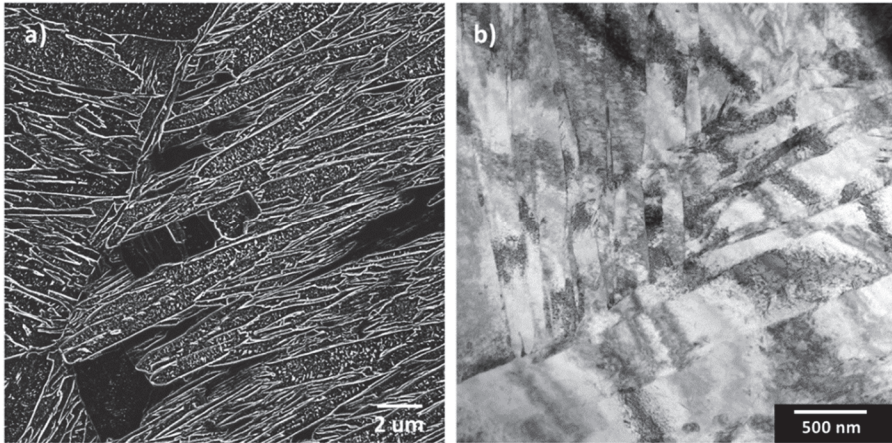


**Fig. 19. Microstructure of the 0.12C steel sample austenitized and quenched at 1000 °C/s. a) SEM Inlens secondary electron (SE) micrograph; b) STEM image from the FIB machined thin foil sample (Reprinted under CC-BY 4.0 license from Paper V © 2020 Authors).**

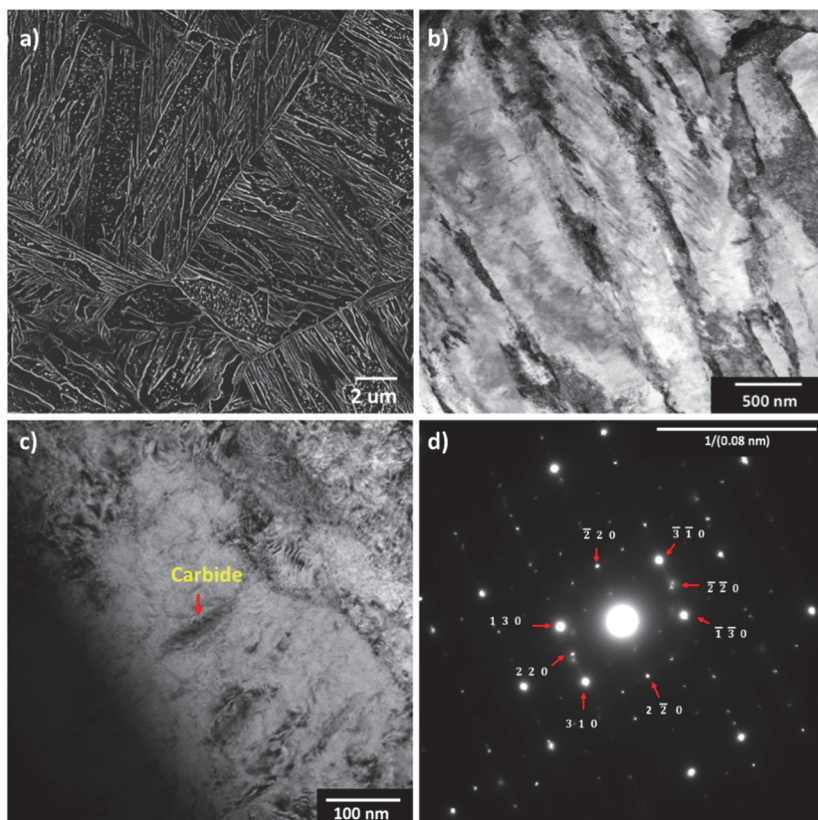


Fig. 20. Microstructure of the 0.12C steel sample austenitized and quenched at 120 °C/s. a) SEM Inlens SE micrograph; b) STEM image from the FIB machined thin foil sample; c) TEM image of the cementite precipitate shown with a red arrow; d) selected area diffraction pattern with spots corresponding to indexed cementite. Cementite zone axis [001] (Reprinted under CC-BY 4.0 license from Paper V © 2020 Authors).

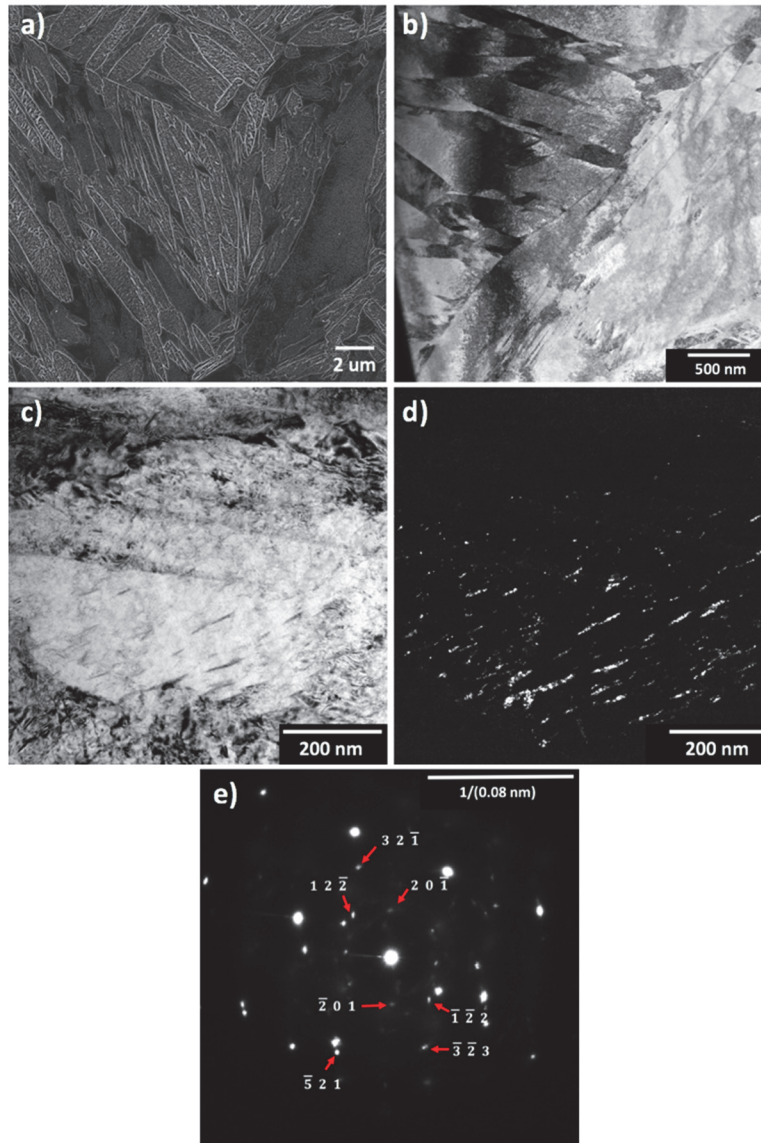


Fig. 21. Microstructure of the 0.23C steel sample austenitized and quenched at 1000 °C/s. a) SEM Inlens SE micrograph; b) STEM image from the FIB machined thin foil sample; c) bright-field TEM image of the cementite precipitates; d) corresponding dark-field image of the cementite precipitates; e) selected area diffraction pattern with spots corresponding to indexed cementite. Cementite zone axis  $[234]$  (Reprinted under CC-BY 4.0 license from Paper V © 2020 Authors).

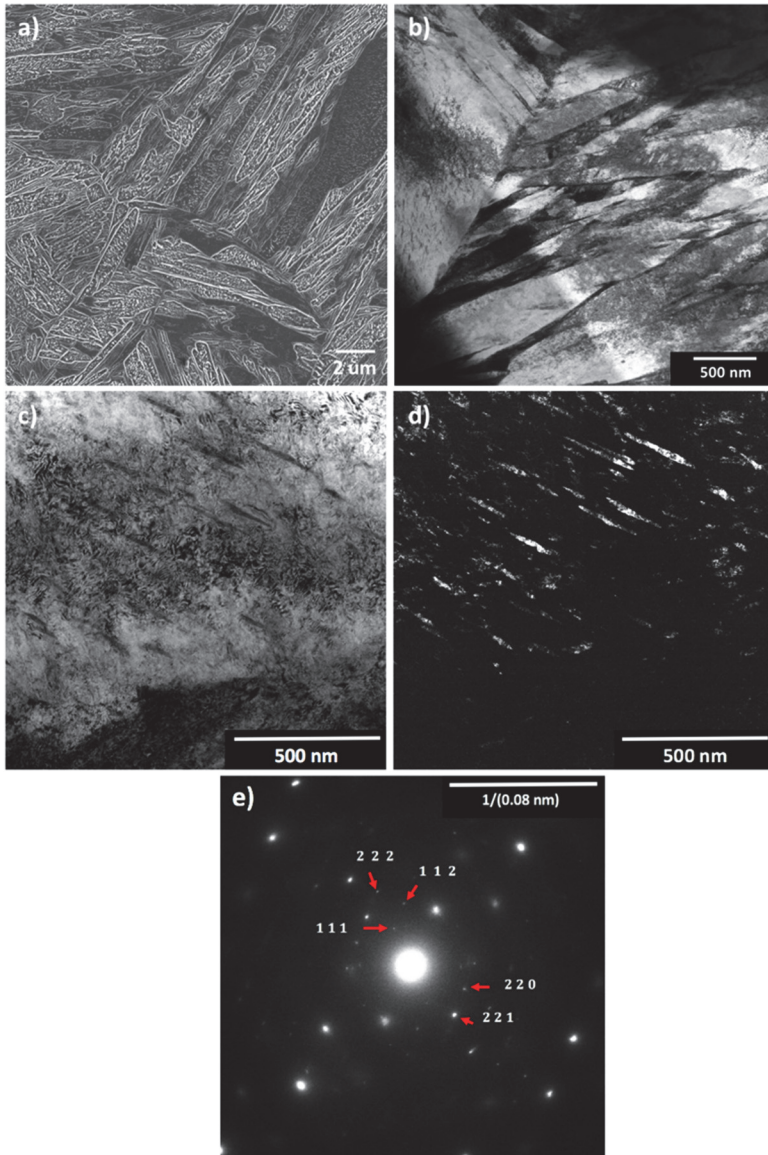
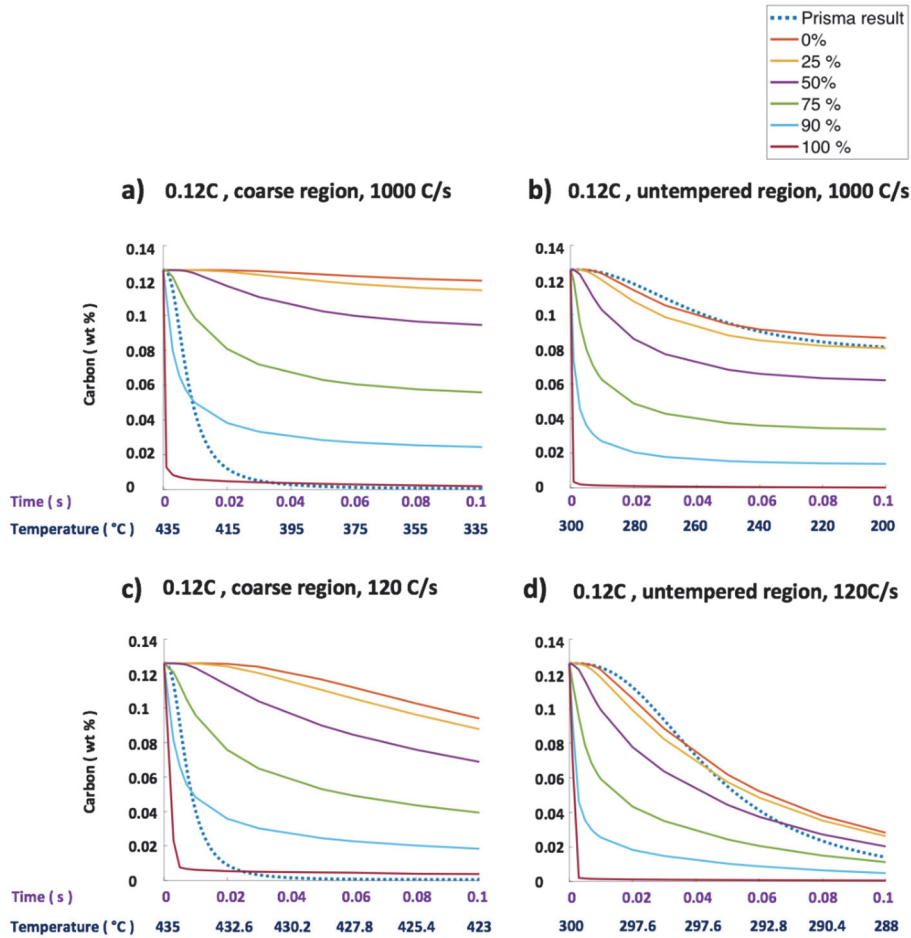


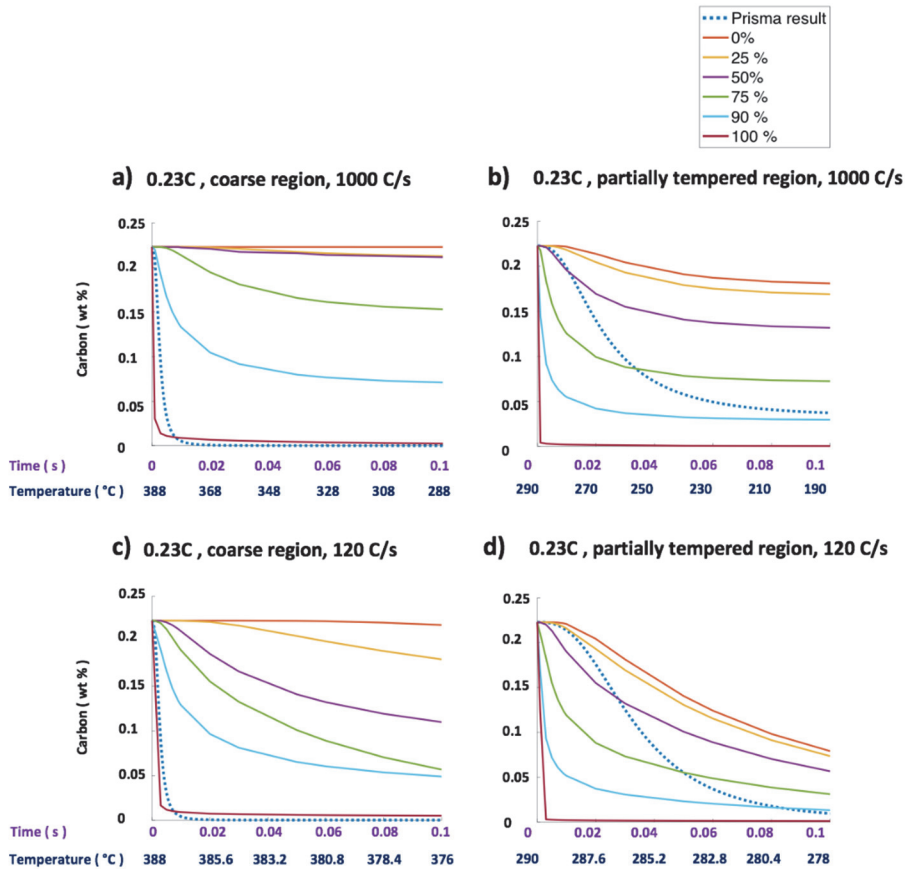
Fig. 22. Microstructure of the 0.23C steel sample austenitized and quenched at 120 °C/s. a) SEM Inlens SE micrograph; b) STEM image from the FIB machined thin foil sample; c) bright-field TEM image of the cementite precipitates; d) corresponding dark-field image of the cementite precipitates; e) selected area diffraction pattern with spots corresponding to indexed cementite. Cementite zone axis [110] (Reprinted under CC-BY 4.0 license from Paper V © 2020 Authors).

Figure 23 shows the carbon depletion rates due to diffusion out of the laths and precipitation within the laths for the 0.12C steel as calculated using the DICTRA and TC-Prisma set-ups, as described in the methodology section. For a cooling rate of 1000 °C/s, except for the carbon content at the 90% and 100% half-thickness locations in the coarse ferrite laths (Figure 23a), the rate of carbon depletion due to precipitation in the matrix is much faster than that due to diffusion into the surrounding austenite. In contrast, Figure 23b shows that the carbon depletion rate due to diffusion from the thin martensite laths, i.e. those formed after 90% transformation, is predicted to be faster than the depletion rate due to precipitation. (In fact, the rate of precipitation will be even lower than that which is shown because it is calculated assuming no loss due to diffusion to the austenite. When the carbon concentration in the matrix is lowered by loss of carbon to the austenite, the driving force for precipitation will be reduced and precipitation slower than that calculated). The carbon depletion rates when quenching at 120 °C/s (Figure 23c and 23d) showed similar results with precipitation being the dominant process in the coarse laths and diffusion to austenite in the thin, last-forming laths.

The carbon depletion rates from ferrite laths to austenite in the 0.23C steel for quenching at 1000 °C/s can be seen in Figure 24a and 24b, and for 120 °C/s in Figure 24c and 24d. The carbon depletion rates in the 500 nm half-thickness coarse region are similar to that of the quenched 0.12C steel, where carbon depletion by precipitation is faster than by diffusion of carbon from the laths for both cooling rates. The main difference is that in the quenched 0.23C steel, the carbon depletion rate due to diffusion is slightly higher only at the 100% and not the 90% half-thickness position. Figure 24b shows that for the 50 nm half-thickness laths formed at 290 °C, the carbon depletion rate due to precipitation is faster than that due to diffusion from ferrite at the 0% and 25% lath positions, but the diffusion of carbon from the ferrite laths is predicted to be faster than precipitation at the 50%, 75%, 90% and the 100% positions. Figure 24c and 24d shows that similar results are obtained for quenching at 120 °C/s, with the only difference being that there is an increase in the loss of carbon due to diffusion into austenite.



**Fig. 23.** Comparison of the rate of carbon depletion from the lath matrix by diffusion into austenite and by precipitation of cementite in a time span of 0.1 s from the instant of lath formation for the 0.12C steel. a) 1000 nm thick lath formed at 435 °C, cooling rate is 1000 °C/s. b) 100 nm thick lath formed at 300 °C, cooling rate is 1000 °C/s. c) 1000 nm thick lath formed at 435 °C, cooling rate is 120 °C/s. d) 100 nm thick lath formed at 300 °C, cooling rate is 120 °C/s. Abscissa shows time after lath formation and corresponding temperatures (Reprinted under CC-BY 4.0 license from Paper V © 2020 Authors).



**Fig. 24.** Comparison of the rate of carbon depletion from the lath matrix by diffusion into austenite and by precipitation of cementite in a time span of 0.1 s from the instant of lath formation for the 0.23C steel. a) 1000 nm thick lath formed at 388 °C, cooling rate is 1000 °C/s. b) 100 nm thick lath formed at 290 °C, cooling rate is 1000 °C/s. c) 1000 nm thick lath formed at 388 °C, cooling rate is 120 °C/s. d) 100 nm thick lath formed at 290 °C, cooling rate is 120 °C/s. Abscissa shows time after lath formation and corresponding temperatures (Reprinted under CC-BY 4.0 license from Paper V © 2020 Authors).

## 4 Discussion

### 4.1 Influence of microsegregation on the onset of martensite formation

Sourmail and Smanio (2013) pointed out the thermal gradients in dilatometry specimens could result in the cooler regions transforming into martensite earlier than the other regions during cooling. The Gleeble dilatometer measures the change in the diameter of the specimen with respect to the temperature measured on the surface of the specimen of the same section as used to record the specimen diameter. The heat from the sample is removed along the axial direction of the cylindrical specimen. In an ideal scenario, the thermal isotherms should be parallel to the diameter of the specimen so that there is no temperature difference between the centre and the surface. However, radiation leads to heat loss into the vacuum, which results in a radial temperature gradient. Calculations based on the approach as described by Semiatin et al. (2017) showed that in a 6 mm diameter cylindrical specimen, below temperatures close to the  $M_s$ , the maximum steady state temperature difference between the centre and the surface due to radiation losses is less than 0.8 °C. Therefore, the thermal gradients in the studied sample should have a negligible influence on the slow-start phenomenon during the onset of martensite.

The Kung and Rayment empirical formulae used to calculate the  $M_s$  temperature from chemical composition has been modified to fit with the measured dilatational curves. This was expected as there are systematic differences which arise when using the original formula developed under specific experimental conditions with the current problem. Austenite grain size is known to influence  $M_s$ . An increase in the austenite grain size leads to an increase in the  $M_s$  temperature, as pointed out by Yang and Bhadeshia (2009). A variation in austenite grain size can itself cause scatter in local  $M_s$  temperatures. Grain refinement was shown to have shifted the  $M_s$  temperatures to lower values (Celada-Casero et al., 2019). The reduction in grain size increases the grain boundary area per unit volume. This increases the average resistance of the austenite to the plastic deformation required to accommodate the transformation shape strain (Nichol, Judd, & Ansell, 1977; Brofman & Ansell, 1983). Therefore, the required driving force for the formation of the martensite is increased by the additional strain energy arising from the small grains. Lath lengths are limited by the packet size, which in turn is limited by the austenite grain size (Morito et al., 2005). If the length of the lath is approximated

by an oblate spheroid with a thickness of  $2c$  and a length of  $2a$ , the decreasing packet and grain size leads to increasing  $c/a$  ratios. This leads to additional transformation strain energy in the smaller grain over that which is needed for the transformation into a coarse austenite grain. Grain size differences are expected to reflect in the magnitude of the constant  $a_0$  in the Kung and Rayment regression equation. In the studied sample, the average ECD of the austenite grains was found to be  $15\ \mu\text{m}$  with a standard deviation of about  $8\ \mu\text{m}$  (Paper I). The maximum ECD was measured to be  $37\ \mu\text{m}$  (Paper I). However, it was pointed out that such scatter can explain only about  $4\text{--}5\ ^\circ\text{C}$  of the slow start (Sourmail & Smanio, 2013). This cannot explain the full  $31\ ^\circ\text{C}$  temperature range of the slow start as measured in the current study.

As seen in Table 3, the effect of variations in the Cr content of the 12Cr steel is five times higher than the next most significant alloying element, i.e. Mn. Therefore, the Kung and Rayment regression coefficients for C, Mn, Si and Ni will not significantly affect the temperature range of the slow-start, but they have an effect on the absolute  $M_s$  temperatures. Therefore, the approach of only considering the possible errors in the coefficients of  $a_0$  and  $a_{Cr}$  can be justified. The difference between the modified and the original value for  $a_0$  was found to be only  $1\ ^\circ\text{C}$ . This considers the effects of grain size variance and for errors in the coefficients  $a_C$ ,  $a_{Mn}$ ,  $a_{Si}$ ,  $a_{Ni}$  and  $a_{Mo}$ . The modified value for  $a_{Cr}$  makes the predicted slow-start dilatation curve a better fit with the experimental data. It was found that the modified value  $a_{Cr}$  was  $-6.43$  as opposed to the original value which was  $-12.1$ . This means that the slow start temperature range can be explained well within the observed variations of the Cr alloying element content. The original value for  $a_{Cr}$  would have predicted a much slower start during the onset of the martensitic transformation.

Despite the fact that the amplitude of the interdendritic microsegregation concentration profiles are reduced during the cooling of the cast material and the subsequent reheating prior to rolling, after rolling reductions of 14, significant differences still remain in the finished plate. The leanest local compositions in the studied steel had the highest calculated  $M_s$  temperatures of about  $20\ ^\circ\text{C}$  more than the mean. This explains the earlier slow start of the martensite transformation. Therefore, as seen in Figure 8, the first martensite transformation occurs in the lean alloyed regions after which the other regions contribute to the increasing martensite fraction. The lean alloyed regions only affect the first 10% of transformation. After that, the martensite fraction calculated using the K-M equation based on the mean composition is almost identical to that calculated using the 100 individual local compositions measured with EPMA. With these results, the theoretical curves, as

seen in Figure 9, can help in precise quantitative predictions of the  $M_s$  temperatures. The dispersion of  $M_s$  temperatures due to microsegregation can be related to the gradual slope change during the onset of the martensite transformation.

Formulating a close-form equation which includes the gradual slow start during the onset of martensite transformation is beneficial as such an equation can be readily implemented in simulation software. The existing K-M equation was reformulated by considering the inhomogeneities in the chemical composition, as shown in Paper I. The reformulated equation is

$$\langle f_m(T_q, \mu, \sigma) \rangle = \begin{cases} \frac{\alpha(\mu + \sqrt{3}\sigma - T_q) - f_m(T_q, \mu + \sqrt{3}\sigma)}{2\sqrt{3}\sigma\alpha}, & \mu - \sqrt{3}\sigma \leq T \leq \mu + \sqrt{3}\sigma \\ 1 + \frac{f_m(T_q, \mu - \sqrt{3}\sigma) - f_m(T_q, \mu + \sqrt{3}\sigma)}{2\sqrt{3}\sigma\alpha}, & T < \mu - \sqrt{3}\sigma \end{cases}, \quad (6)$$

where the new terms introduced are  $\mu$ , the mean value of the  $M_s$ ,  $\sigma$ , the standard deviation of  $M_s$  values calculated from measured or predicted local variations in chemical composition, and  $T_q$  is the temperature at which the martensite fraction is calculated. The main difference between the numerical integration of the martensite evolution based on the 100 EPMA compositions and the proposed formula was that in the new formulation, the  $M_s$  temperatures are assumed to be uniformly distributed in the range  $\mu - \sqrt{3}\sigma \leq T \leq \mu + \sqrt{3}\sigma$ , i.e. between points ‘a’ and ‘b’ in Figure 8, while experimental results, as seen in Figure 8, show a broader distribution.

## 4.2 Tempering during hot mounting

The coarse and fine lath regions observed in the SEM micrograph of the 0.12C steel sample quenched at 1000 °C/s, as seen in Figure 10, are commonly found in as-quenched low-alloy steels, as also observed by Morsdorf et al. (2015, 2016). It was suggested that the coarse laths are the first martensite features which form just under the  $M_s$  temperature because the resistance to the growth of the coarse martensitic regions is small due to the effect of high temperature on the strength of the austenite.

The high density of carbides in the coarse martensitic regions would suggest that the early coarse martensite formation, which transforms from austenite just below the  $M_s$  temperature (435 °C in the 0.12C steel), is accompanied by auto-tempering. The precipitated carbides had rod- or plate-like shapes and were

identified as cementite using TEM. Epsilon or Hägg carbides were not found in either the cold- or hot-mounted specimens despite the fact that it has been shown that tempering at 180 °C can result in the precipitation of epsilon carbides in steels with more than 0.2 wt.% C (Speich, 1969).

The fast quenching causes a higher cooling rate at the surface compared to the centre of the specimen, giving a radial temperature gradient. This means that martensite first forms near the surface. Irrespective of the location, the auto-tempering depends on the cooling rate after the first martensite is formed and not on the temperature gradient. The dark regions with negligible to no precipitation are present throughout the cold-mounted specimen irrespective of the different cooling rates experienced at the centre or near the surface of the specimen. However, in the hot-mounted specimens, the darker regions showed a discernible amount of precipitation throughout the specimens. Therefore, additional tempering occurs during hot mounting: the observations are not due to variation in the locations of the areas studied.

### **4.3 Relationship between crystal orientation and auto-tempering**

As explained earlier, the formation of coarse laths is favourable at temperatures just under  $M_s$  as the austenite matrix is relatively soft with a low defect density in the undeformed specimen. Naturally, the coarse regions could simply be thin laths intersected at small angles at the specimen surface. But Morsdorf et al. (2015) showed that the coarse regions are thicker than the surrounding thin laths using 3D sectioning techniques. The degree of auto-tempering is higher within the coarse regions as the high atomic mobility at temperatures just below the  $M_s$  is beneficial for the nucleation and growth of cementite. After the formation of the coarse regions, the combination of falling temperature and the plastic accommodation of the already formed martensite results in an increase in the dislocation density of the austenite (Morsdorf et al., 2015). This leads to progressive hardening of the untransformed austenite, which is followed by the formation of the fine lath ridge-like martensite regions. The untempered regions transform at lower temperatures close to the martensite finish temperature. The untempered regions appear with a plateau-like flat topography due to a lack of etching in Nital.

The EBSD results seen in Figures 13 and 14 show that irrespective of the grain sizes, the last formed untempered martensitic regions had orientations with or close to  $\{100\}/ND$ . It was pointed out by Reisinger et al. (2017) that surfaces parallel to the  $\{100\}$  planes etch more slowly when compared to surfaces which are parallel

to other planes. However, the above reason does not explain the lack of etching in the untempered regions as the specimens have been sectioned perpendicular to the plate RD. As seen in Figure 25a, the untempered regions are red, i.e. they are oriented in such a way that their  $\{100\}$  planes are parallel to the plate ND. However, the etching response of the grains will be affected by the crystallographic orientation of the RD since the cross-sections are made normal to RD. Figure 25b shows that the same untempered regions are cut so that the crystallographic orientation of their surface planes is something other than  $\{100\}$ . This indicates that the lack of etching seen in the untempered regions is not due to them having  $\{100\}$  parallel to the etched surface.

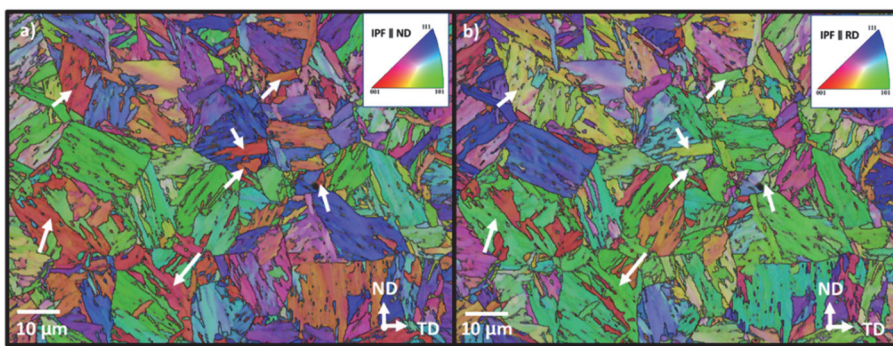


**Fig. 25. EBSD IPF maps of small grains in the 0.12C steel which was austenitized for 24 hours and quenched, as seen on a cross-section normal to plate RD. a) Crystallographic directions of the plate normal direction (ND) and b) crystallographic directions of the plate rolling direction (RD). The white arrows point to the relatively untempered dark regions (Reprinted [adapted] under CC-BY 4.0 license from Paper III © 2019 Authors).**

Hot mounting was shown to cause the appearance of carbides in the relatively dark regions, as described earlier, while no visible carbides could be seen in the dark untempered regions of the cold-mounted specimens. This indicates that the untempered regions etch slowly due to supersaturation of carbon in the matrix.

Bearing in mind the fact that the effective grain size for cleavage fracture in lath martensitic steels is the orientation and coherence length of the  $\{100\}$  cleavage crack planes (Morris, Kinney, Pytlewski, & Adachi, 2013), the orientation of the untempered martensitic regions being close to  $\{100\}$ //ND is significant with regard to the toughness of as-quenched martensitic steels, especially when loaded in the through-thickness direction.

It can be seen from the results illustrated in Figures 15 and 16 that the apparent selection of variants cannot be explained by comparing with immediate neighbours. The untempered regions are a single block and can be considered as part of the larger packet structure, which generally also consists of coarse auto-tempered and ridge-like regions. Calculations by Morito et al. (2003) show that the variant pair combinations within a single packet reduced the total shape strain by the process of self-accommodation. Therefore, assuming that the untempered regions are the last to transform into martensite, the variant pairs in the untempered regions ought to be selected by the principle of minimization of transformation strains due to self-accommodation. This hypothesis has not been investigated in this study and requires further research.

#### **4.4 Image processing toolbox**

It has been demonstrated that the apparent volume fraction of carbides in auto-tempered microstructures can be determined from SEM micrographs of as-quenched low-carbon martensitic steels using the MATLAB image processing program developed as a part of this thesis. It is not possible to calculate the error associated with an image as the limiting factors are the resolution of the SEM micrograph and the binary image as computed by MATLAB. The qualitative volume fraction can either be obtained from one image or multiple images if the volume fraction over a large area should be determined. The information from three images giving 30000 discretized boxes was sufficient to get a good overall estimation of the degree of auto-tempering as the carbides in auto-tempered microstructures were evenly distributed in the samples.

The overestimation in the calculated volume fraction can be explained by the following two factors: 1) some rod-like shaped cementite particles are smaller than the pixel size and 2) the cementite precipitates project out of the etched surface at various angles, as can be seen in Figure 26. The dimension " $d_c$ " which is required for calculating the area/volume fraction appears larger than " $d_a$ ". Also, the apparent size of small objects is larger than they actually are due to the finite size of the electron beam producing a secondary electron signal outside the centre-point of the beam. This effect defines the resolution limit of the microscope under the beam conditions used to obtain the image. Due to the cleanness of the studied steel, non-metallic inclusions do not influence the calculated volume fraction. Further improvements can be made in code by removing a minimum value below which all

pixels are considered as noise. However, this only led to a 0.3% reduction from the calculated volume fractions. Therefore, the qualitative comparisons do not change.

The apparent carbide volume fraction can still provide useful qualitative information about the local area fraction of the carbides in auto-tempered microstructures despite the drawbacks stated above. This was demonstrated by comparing the results from the 0.12C steel sample quenched at 100 °C/s with another sample of the same composition which was quenched at 1000 °C/s, as described in the methodology section. The SEM micrograph of the 1000 °C/s specimen can be seen in Figure 27a. Visually, it can be seen that the carbides are not as abundant when compared to the 100 °C/s quenched specimen, as seen in Figure 17. By the method of image segmentation described in the methodology section, the carbides were isolated from the other features and the apparent volume fraction of the carbides in auto-tempered microstructures was calculated to be 2.74%. This was a reduction of 0.28% when compared to the apparent fraction determined in the sample quenched at 100 °C/s. The corresponding colour map seen in Figure 27b shows the apparent local area fraction of the carbides in auto-tempered microstructures. The histogram seen in Figure 28 qualitatively compares the relative local apparent area fractions of the carbides in auto-tempered microstructures from both specimens. The brown bars represent the apparent fractions calculated for the specimen quenched at 1000 °C/s and the blue bars represent the fractions from the specimen quenched at 100 °C/s. The histogram data was constructed from three images, which amounts to 30000 indexed boxes. The < 1% apparent area carbide fraction bars from both samples were almost identical. The 100 °C/s specimen histogram showed a higher bar for the > 10% local area carbide fraction. This is expected as the lower cooling rate allows more time for carbides that precipitate close to  $M_s$  to become denser and larger. The specimen quenched at 1000 °C/s shows a higher bar for the 1–10% apparent carbide fractions. This proportion is higher because, as expected, the carbides which precipitate at the higher cooling rate are smaller than the ones which form at a slower rate.

This demonstrates that the custom-built image processing program can be used to qualitatively compare and estimate the apparent auto-tempered volume fractions in as-quenched low-carbon martensitic steels.

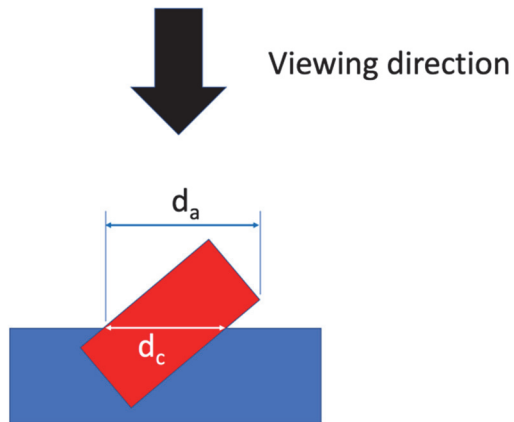


Fig. 26. Schematic cross-section through a polished and etched surface showing the carbide dimension that would lead to a correct estimate of the carbide volume fraction ( $d_c$ ) and the corresponding apparent dimension ( $d_a$ ) seen projected onto the plane of the scanned SE image (Reprinted under CC-BY 4.0 license from Paper IV © 2020 Authors).

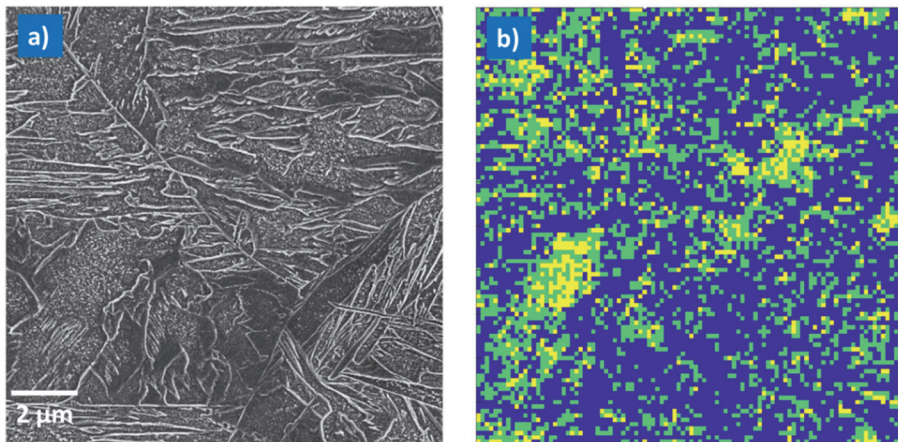
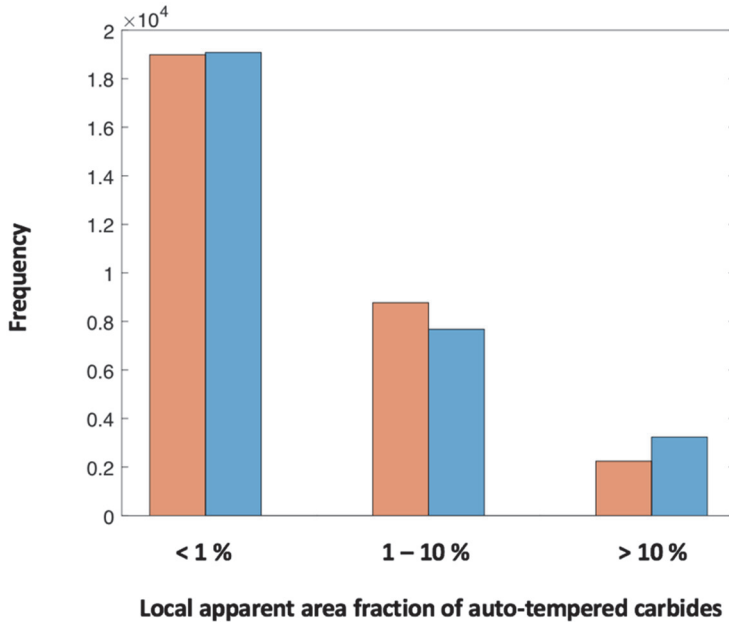


Fig. 27. a) SEM image of the 0.12C steel sample which was austenitized and quenched at 1000 °C/s. b) Through the use of the custom-built MATLAB computer program, a colour map that indicates the local area fraction of carbides in auto-tempered microstructures within the highly auto-tempered regions. Apparent area fractions of carbides in auto-tempered microstructures: > 10% yellow, 1–10% green and < 1% blue (Reprinted [adapted] under CC-BY 4.0 license from Paper IV © 2020 Authors).



**Fig. 28.** Histogram of local apparent area fraction of carbides in auto-tempered microstructures from the quenched 0.12C steel. Blue bars are specimens cooled at 100 °C/s and brown bars are the specimens cooled at 1000 °C/s (Reprinted under CC-BY 4.0 license from Paper IV © 2020 Authors).

#### **4.5 Kinetics of auto-tempering and auto-partitioning during quenching**

It is interesting to compare the SEM micrographs of the coarse auto-tempered regions and the thin laths (Figures 19–22) with the simulation results seen in Figures 23 and 24. Figure 29 compares the predicted carbon concentration profiles when the 50 nm ferrite half-thickness lath formed at 290 °C in the 0.23 C steel is adjacent to two different austenite thicknesses. For the cooling rate of 1000 °C/s seen in Figure 29a and 29b, irrespective of the assumed austenite thickness in the range 5–50 nm, it can be seen that the carbon concentration profiles in ferrite and austenite are identical. This is because the carbon concentration profiles deviate from the bulk content only to a depth of around 3 nm. For the cooling rate of 120 °C/s, Figure 29c and 29d shows that the concentration profile deviates from

the bulk concentration to a depth of about 7 nm when the austenite cell thickness is 50 nm. Because of this, the far-field carbon concentration rises to about 2 wt.% when the austenite cell is only 5 nm thick. However, despite this, there was almost no difference in the ferrite carbon concentration profiles between the two austenite thicknesses. Therefore, the simulation results are independent of the choice of austenite thickness in the range 5–50 nm.

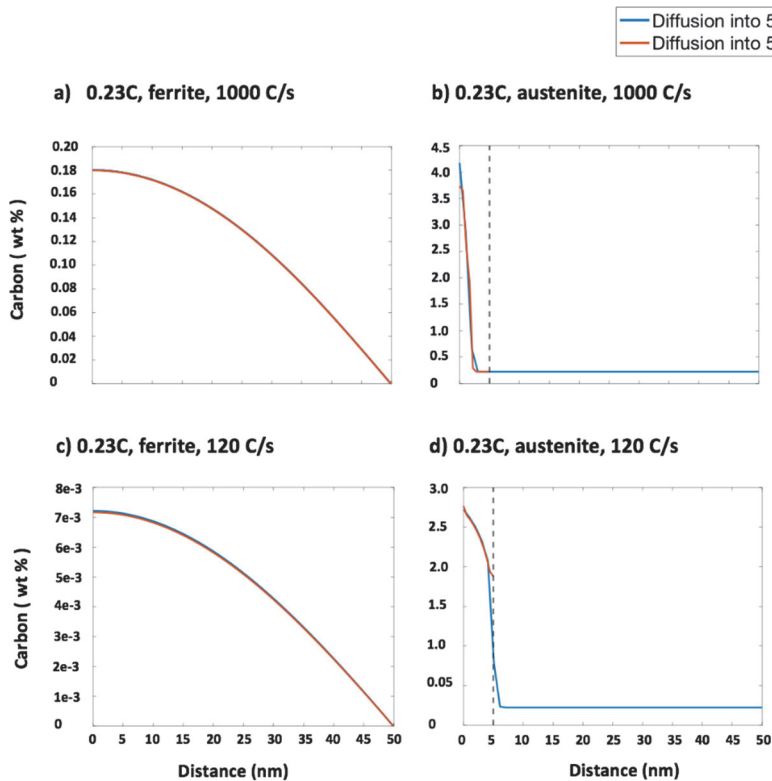


**Fig. 29.** Comparison of the predicted as-quenched carbon concentration profiles for two austenite thicknesses adjacent to a lath which has formed at 290 °C in the 0.23C steel. a) and b) 1000 °C/s, c) and d) 120 °C/s. Ferrite given in a) and c). Austenite given in b) and d). Note scale changes. The dashed lines in the austenite profiles represent the 5 nm austenite thickness (Reprinted under CC-BY 4.0 license from Paper V © 2020 Authors).

Martensite has been reported to form at high speeds (Bhadeshia & Honeycombe, 2017). Therefore, the assumption that the martensite has formed instantaneously is

reasonable. Despite the formation of neighbouring martensite, the laths are assumed to be surrounded by austenite during the quenching process. Figure 30 shows that there is an interlath austenite film around the martensite lath present after quenching at room temperature. Therefore, the lath can be kept adjacent to a constant half-width thick austenite and the changing environment further away can be ignored. The only condition is that the adjacent austenite should either be thick enough to retain the carbon concentration at the far wall of the calculation cell at the bulk carbon concentration or that the carbon concentration at the far wall only rises to such an extent that it does not cause significant errors in the adjacent ferrite. These values have been calculated and are given in Table 9.

**Table 9. Minimum austenite thickness needed to accommodate the carbon concentration profiles (Reprinted under CC-BY 4.0 license from Paper V © 2020 Authors).**

Steel Code	0.12C				0.23C			
	120		1000		120		1000	
Cooling rate (°C/s)	435	300	435	300	388	290	388	290
Lath formation temperature (°C)	70	5	35	5	55	5	20	5
Minimum austenite half-width (nm)								

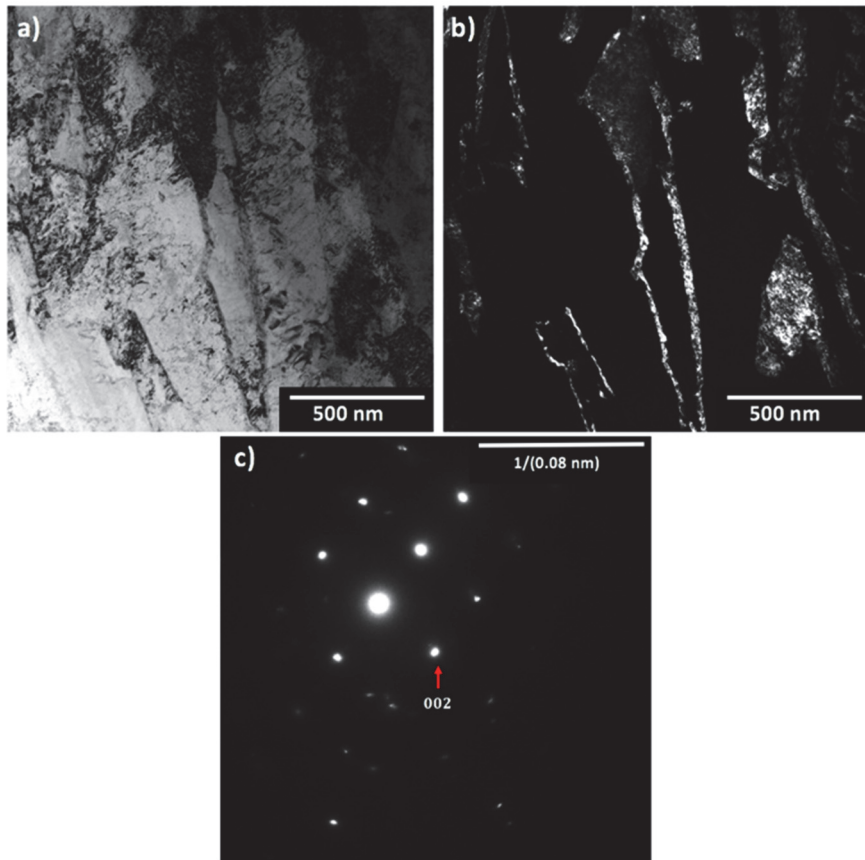


**Fig. 30.** Microstructure of the 0.12 C steel which was austenitized and quenched at 1000 °C/s. a) Bright-field TEM image showing martensitic laths; b) corresponding dark-field image with retained austenite indicated by the bright regions; c) SAD pattern showing the indexed austenite spot indicated by the red arrow (Reprinted under CC-BY 4.0 license from Paper V © 2020 Authors).

The predictions for the 0.12C steel quenched at 1000 °C/s seen in Figure 23a,b correspond well with the SEM micrograph in Figure 31a, showing that the precipitation of a high density of carbides is favourable in the coarse martensitic region. There was a narrow precipitate-free zone which is adjacent to the coarse region boundary (corresponding to 90% width), as indicated by red arrows in Figure 31a. This zone was predicted in Figure 23a, which shows that at the 90% thickness position, the carbon depletion rate due to diffusion into austenite is faster than when compared to the precipitation of carbides. The thin precipitate-free laths

seen in Figure 31a also correspond well with the predictions in Figure 23b, which show that the diffusion of carbon from ferrite into austenite is faster than by precipitation in the laths which have formed at lower temperatures. Similar observations can be seen when the simulation results of the 120 °C/s cooled specimens in Figure 23c and 23d are compared with the SEM micrograph in Figure 32b.

The SEM micrographs of the 0.23C steel sample quenched at 1000 °C/s seen in Figure 31c, which shows the precipitates distributed throughout the coarse lath, also correspond with the simulation results seen in Figure 24a. It can also be seen that there is no distinct precipitate-free region near the coarse region boundaries. This corresponds with the simulation results, which show that beyond the 90% half-thickness region, the precipitation dependent carbon depletion rate is faster than the depletion rate due to diffusion through the thickness of the coarse lath. Very small precipitates can be found throughout the relatively dark regions that have transformed at low temperatures. This is at odds with the simulation results seen in Figure 24b, which show that the carbon depletion rate due to precipitation is faster than by diffusion near the centres (25% thickness positions) and not throughout the thickness of the thin laths. One reason could be that there is still a significant carbon concentration remaining in the ferrite even after diffusion into the austenite (Figure 32). This supersaturation in the matrix might be enough to promote the growth of carbides throughout the dark region.

The coarse auto-tempered region in the 0.23C steel sample quenched at 120 °C/s seen in Figure 31d can be predicted by the simulation results seen in Figure 24c. It was also seen that narrow precipitate-free regions can be seen near some coarse region boundaries but not at others. This is due to the fact that the diffusion of carbon into austenite is expected to affect precipitation to a greater depth when compared to 1000 °C/s.

Except for a low density of small precipitates in the middle, the narrow laths appear to be precipitate-free, as seen in Figure 31d. This matches the predicted simulation results seen in Figure 24d, where the carbon depletion rate due to precipitation from the matrix is much faster in the middle of the thin lath while diffusion into austenite is faster above 50% of the half-thickness of the thin ferrite laths.

These results show that the approximate simulation calculations using DICTRA and TC-Prisma can sufficiently predict the phase transformations in as-quenched low-carbon martensitic steels.

In the light of the above results, which were documented in Paper V, the simulations on how the hot mounting affects the 0.12C steel samples quenched at 1000 °C/s, as seen in Paper II, has been updated in this thesis. DICTRA was used to simulate the growth of cementite in the untempered martensite regions during the hot-mounting stage, using the set-up shown in Figure 3. The approximations are described in the methodology section. The carbon content predicted to remain at the various positions through the ferrite half-thickness after quenching to room temperature (Figure 32) served as the initial values for the simulations (Figure 33a). The predicted cementite radius after the hot-mounting thermal cycle can be seen in Figure 33b. Naturally, the cementite radius was predicted to be the largest at the 0% lath position and smallest at the 100% lath position. This is to be expected as the final cementite radius growth is dependent on the amount of carbon at different ferrite lath positions. The DICTRA-predicted values differed only by 0.1% volume fraction when compared to the TC-Prisma calculations, which also consider the incubation time.

The DICTRA calculations imply that the hot mounting thermal cycle can cause the carbon surrounding any pre-existing precipitates or nuclei to grow to a size corresponding to almost the full equilibrium volume fraction. This prediction is supported by the experimental results, which show that hot mounting changes the appearance of the dark unprecipitated regions of the auto-tempered martensite.

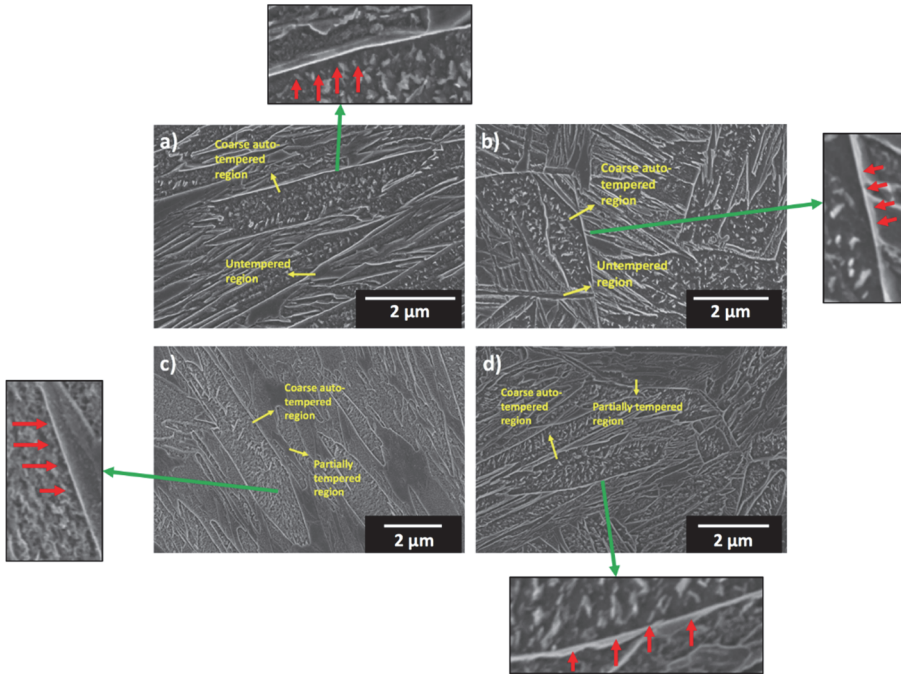


**Fig. 31. SEM micrographs showing auto-tempered and relatively untempered martensitic laths in a) 0.12C steel, quench rate: 1000 °C/s; b) 0.12C steel, quench rate: 120 °C/s; c) 0.23C steel, quench rate: 1000 °C/s; d) 0.23C steel, quench rate: 120 °C/s. The green arrows point to close-ups of the coarse regions. The red arrows indicate the lath boundaries. A distinct precipitate-free region at the coarse region boundaries can be seen in the quenched 0.12C steel. A similar boundary is either not present or is very thin in the quenched 0.23C steel (Reprinted under CC-BY 4.0 license from Paper V © 2020 Authors).**

The hardness results show that there was a statistically significant increase in the measured hardness due to hot mounting. The additional tempering due to hot mounting can increase the contribution of the precipitation hardness in the sample. However, factors such as the decrease in the solid solution strengthening due to the loss of interstitial carbon from the bcc martensite matrix also exist. Also, it is unclear how the hardness contributions from grain and lath boundaries change during the hot-mounting cycle. Due to the complicated nature of the factors contributing to the strength and hardness of martensite, the reasons for the increase in the hardness of the untempered regions has not been explored in this thesis project.

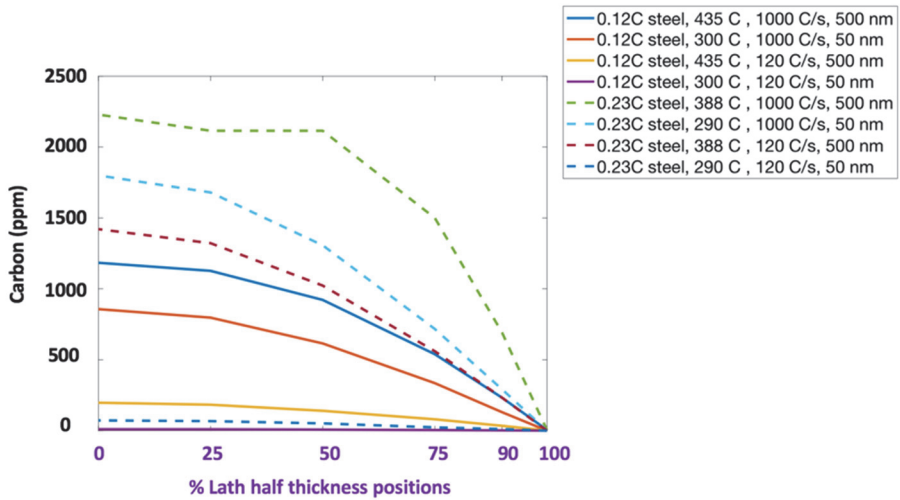


**Fig. 32. Predicted carbon content (ppm) remaining in ferrite at room temperature (23 °C) after diffusion of carbon into austenite with the assumption that there is no carbide precipitation. The 0% and 100% positions indicate the centre and the interface between ferrite and austenite, respectively. The key gives the steel codes, lath formation temperatures, subsequent cooling rates and the lath half-thicknesses (Reprinted under CC-BY 4.0 license from Paper V © 2020 Authors).**

The above calculations concerned the 0.12C steel quenched at 1000 °C/s. Untempered regions can also be found in the 0.12C steel samples quenched at 120 °C/s. It can be seen from Figure 32 that in the case of this cooling rate, a negligible concentration of carbon is predicted to remain in the thin laths at room temperature. Therefore, the calculations imply that there would be no carbide precipitation during subsequent hot mounting as there is not enough carbon in the untempered regions to promote carbide formation. The electron micrographs in Figure 34 support this prediction as there is no discernible difference between the untempered regions of hot- and cold-mounted specimens. Therefore, both the simulations and experiments show that hot mounting has no visible effect on the untempered lath regions in the 0.12C steel quenched at 120 °C/s.

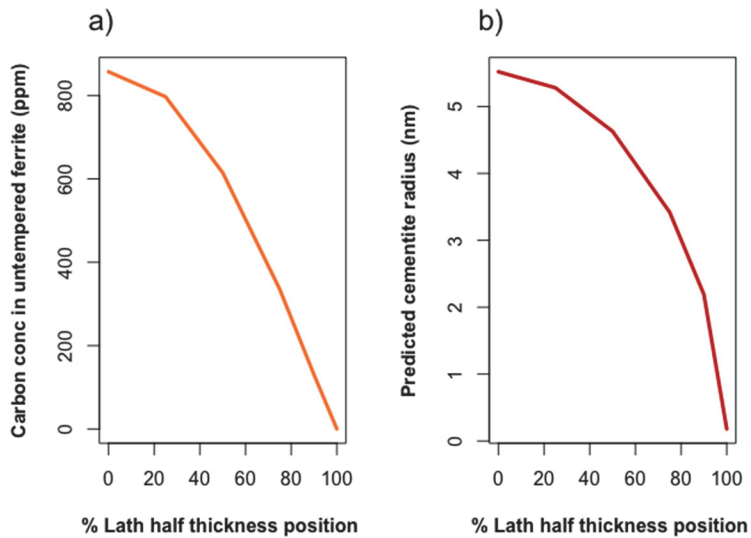


**Fig. 33. a) Carbon levels in the untempered martensite lath with a half-thickness of 50 nm after cooling at 1000 °C/s. b) Predicted radius to which a cementite precipitate would grow as a result of the hot mounting thermal cycle (180 °C for 4 minutes) for the carbon concentrations given in a) assuming no interaction between the slices at the 0, 25, 50, 75, 90 and 100% positions. The 0% and 100% positions indicate the centre of the 50 nm thick lath and the interface between ferrite and austenite, respectively.**

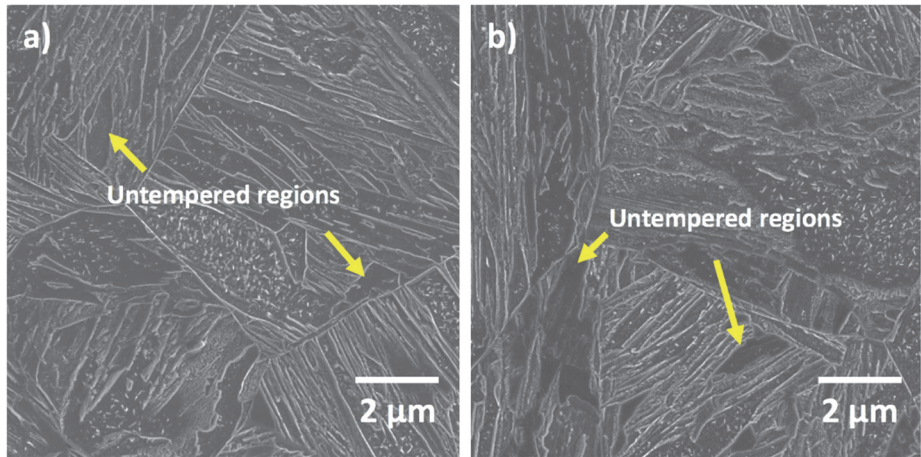


**Fig. 34. SEM micrographs of the 0.12C steel specimen which was austenitized and quenched at 120 °C/s. a) Cold-mounted. b) Hot-mounted. Arrows indicate untempered regions.**

## 5 Summary and conclusions

The thesis has been summarized and conclusions drawn under the following headings: i) Influence of microsegregation on the gradual onset of martensitic transformation, ii) Effects of hot mounting on the microstructure of as-quenched low-alloy martensitic steels, iii) Relationship between crystal orientations and auto-tempering levels in as-quenched low-alloy martensitic steels, iv) Image processing tool to quantify carbides in auto-tempered microstructures in as-quenched low-alloy martensitic steels and v) Comparison of precipitation and partitioning kinetics which occur during quenching of low-alloy martensitic steels.

### 5.1 Influence of microsegregation on the gradual onset of martensitic transformation

The cause for the dispersion of  $M_s$  temperatures which results in a gradual onset of martensite was investigated. A high hardenability 12Cr stainless steel was processed in a Gleeble thermomechanical simulator which was equipped with a dilatometer. The EPMA was used to quantify the chemical inhomogeneity by measuring 100 equidistant local compositions along a distance of 1 mm on the transverse section of the steel specimen. The  $M_s$  temperatures were calculated from all the local compositions and the average martensite fraction vs temperature was determined using the K-M equations. This resulted in a gradual onset of the martensitic transformation as opposed to a sharp onset which is predicted for a homogeneous composition equal to the mean composition of the steel. The corresponding predicted dilatation curve fit well with the experimentally measured curve. This showed that chemical inhomogeneity can completely explain the gradual onset of the martensitic transformation.

The K-M equation was reformulated into a closed-form solution considering the chemical inhomogeneity. This allows for straightforward calculation of martensite evolution with a gradual onset. The assumption for the reformulated K-M equation is that the  $M_s$  temperatures are uniformly distributed between the upper and lower values calculated from the mean and the standard deviation of the local  $M_s$  temperatures.

## **5.2 Effects of hot mounting on the microstructure of as-quenched low-alloy martensitic steels**

The mounting effects on the 2% Nital etched microstructure of the 0.12C steel sample quenched at 1000 °C/s was investigated using SEM. There was a denser distribution of precipitates within the dark-etching regions of the hot-mounted specimen compared to the cold-mounted specimen, in which the dark-etching regions showed minimal to no precipitates. This shows that the thermal cycle during the hot mounting of the specimen causes additional low-temperature tempering. The hot-mounted specimen also showed a small but statistically significant increase in the measured hardness. The DICTRA simulation also shows that the hot mounting thermal cycle can cause the diffusion of almost all carbon remaining in the last formed regions to cementite.

Electron micrographs from both the cold-mounted and hot-mounted 0.12C steel samples quenched at 120 °C/s showed no discernible difference between the untempered regions. This is because there was negligible carbon remaining in the last-formed martensitic regions after a quench rate of 120 °C/s. Therefore, there is not enough carbon to promote the growth of cementite during the hot-mounting cycle.

## **5.3 Crystal orientations of the last formed martensitic regions in as-quenched low-alloy martensitic steels**

A 0.12C steel specimen was austenitized for 24 hours to obtain a bimodal prior-austenite grain distribution and then quenched to obtain the auto-tempered martensitic microstructure. A SEM investigation revealed that the martensite could be divided into three distinct morphologies which form at successively lower temperatures during the quench to room temperature. They are 1) auto-tempered regions which comprise wedge-shaped, deeply etched coarse martensite with intra-lath cementite precipitates, 2) ridge-like regions which comprise fine laths and 3) featureless untempered regions without visible carbides.

Irrespective of their location in the plate, in both small and large grains (17 μm to 289 μm), the coarse auto-tempered and the ridge-like regions are oriented in the window  $\{111\}/ND$  to  $\{112\}/ND$ . However, the untempered regions with no visible carbides were oriented towards or close to  $\{100\}/ND$ . There were also slightly tempered regions containing small carbides which had the approximate orientation of  $\{103\}/ND$ .

Martensite variant analysis revealed that the untempered regions are single blocks and are generally part of the same packet as the adjacent coarse auto-tempered and ridge-like regions. It is possible that the martensite variant pairs within the untempered regions have formed preferentially by self-accommodation so as to minimize the transformation strains.

#### **5.4 Image processing tool to quantify carbides in auto-tempered as-quenched low-alloy martensitic steels**

A MATLAB-based custom-built image processing program was used to estimate the fraction of carbides in auto-tempered microstructures in the 0.12C steel samples quenched at 100 °C/s. The SEM micrographs were binarized by the program so that the boundaries and precipitates are intensified and the background is set to zero intensity. The grain and lath boundaries were then removed from the binarized SEM image by applying an appropriate threshold pixel number. The resulting image comprised precipitates, i.e. groups of pixels smaller than the threshold number. The binarized image can also be further processed into a colour map showing the apparent local area fractions of carbides in auto-tempered microstructures, e.g. high (> 10%), low (1–10%) and non-tempered regions (< 1%). The program was successfully demonstrated by comparing with the 0.12C steel samples quenched at 100 and 1000 °C/s.

#### **5.5 Comparison of precipitation and partitioning kinetics occurring during quenching of low-alloy martensitic steels**

Two low-alloy 0.12C and 0.23C steel specimens were each quenched at 120 °C/s and 1000 °C/s to obtain auto-tempered martensite. Thermo-Calc-based TC-Prisma and DICTRA were used to predict the carbon depletion kinetics during quenching due to either cementite precipitation or diffusion to the surrounding austenite. This was done by taking the effects of carbon content, lath thickness and cooling into consideration. Based on SEM micrographs, two 1-D DICTRA geometries were considered: a lath half-thickness of 500 nm, which represents the coarse martensite laths formed close to the  $M_s$  temperature, and a lath half-thickness of 50 nm, which represents thin laths formed after 90% martensite transformation.

For both cooling rates in both the 0.12C and 0.23C steels, the calculated carbon depletion rates indicated that carbide precipitation should dominate over diffusion of carbon into austenite in coarse laths that form close to the  $M_s$  temperature. A

narrow precipitate-free zone adjacent to the lath boundary is predicted in the coarse laths of the 0.12C steel but not in the 0.23C steel. Carbon depletion rates due to diffusion into austenite are predicted to be faster than precipitation in the thin laths of the 0.12C steel quenched at both 120 °C/s and 1000 °C/s. Precipitation is predicted to dominate carbon diffusion to austenite at the centres of the thin laths in the 0.23C steel quenched at both 120 °C/s and 1000 °C/s. Experimental SEM micrographs showed that this was only true for the 120 °C/s quench rate but not for the 1000 °C/s rate, where small carbides were found to have precipitated throughout the last formed laths.

## 6 Novel features

To the best knowledge of the author, the findings stated below are original to this thesis:

- Local chemical inhomogeneity has been found to fully explain the gradual start during the onset of martensite. The K-M equation combined with measured local chemical compositions allows experimental dilatometry curves to be predicted well.
- Hot mounting during metallographic sample preparation of low-carbon low-alloy martensitic steels quenched at the rate of 1000 °C/s can cause tempering additional to the auto-tempering in laths that are free of precipitates after auto-tempering. DICTRA simulations supported the experimental findings. The degree of additional tempering depends on the cooling rate.
- All the untempered regions in the auto-tempered martensitic steel were oriented with the plane normal  $\{100\}$  close to the thickness or normal direction of the steel plates. Variant analysis investigation showed that the untempered regions and the auto-tempered regions are part of the same packet.
- An efficient image processing tool which can qualitatively calculate the auto-tempered carbide fraction from SEM micrographs in as-quenched low-alloy martensitic steels. This is a novel technical implementation for the purpose of characterising carbides within auto-tempered steels.
- The demonstration of the ability of the Thermo-Calc modules DICTRA and TC-Prisma to provide microstructural information regarding carbide precipitation during auto-tempering.



## 7 Future research

The present work extends the understanding of the gradual onset of martensite and the auto-tempering phenomenon which occurs during quenching of low-alloy steels. The chemical inhomogeneity was found to have the most contribution towards the slow-start phenomenon during the onset of martensite. It would be of interest to further develop the methodologies used in the current thesis so as to also include the contributions due to variations in the prior austenite grain sizes.

Currently, there is insufficient information regarding all the strength contributors in the auto-tempered martensite microstructure. A more comprehensive knowledge about the mechanical properties would help in determining the reason for the small but statistically significant increase in hardness of hot-mounted samples when compared to cold-mounted samples. In the light of new upcoming induction surface heat treatment production lines for steel where cooling rates exceed 1000 °C/s, there would be a need to explore new time- and cost-efficient metallographic sample preparation strategies which do not influence the sample microstructure.

The finding that all the untempered regions are oriented close to  $\{100\}$ // ND can further be extended by studying how they plastically deform under mechanical load, considering that the cleavage fracture is the coherence length of the  $\{100\}$  cleavage crack planes. This investigation would help better understand toughness properties of as-quenched low-alloy plates. More investigation regarding the martensite variant pair development and its relations to the different microstructure features during the quenching of low-alloy steels would help in building better computer models which can predict the final microstructures.

The colour maps generated by the image processing toolbox in the current thesis can be compared with micro- and nano-mechanical tests. The colour maps could then be used to qualitatively understand the mechanical properties of the different auto-tempered microstructure features found in the as-quenched low-alloy steel. The image processing toolbox can be further improved by algorithms which identify microstructural features which appear during lower cooling rates ( $< 100$  °C/s), such as bainite and ferrite. This integration would make the toolbox usable for a wider range of thermal cycles.

The major limitation with the precipitation vs partitioning kinetics study during quenching was that the calculations were approximate. TC-Prisma assumed that there is no carbon loss due to diffusion from martensite into neighbouring austenite. A coupled diffusion and precipitation calculator built using the Thermo-Calc based

TC-Python or TC-MATLAB software development kit would enable better predictions. The calculator could also be extended to quench and partitioning heat treatment cycles.

An interesting observation from electron micrographs was the presence of twin omega-phase in the quenched low-alloy steels. There is a limited understanding as to how the twins form and how they are affected by the quench rates. Further studies are required to understand them and determine their influence on the final properties of the steel.

## List of references

- Andersson, J. O., Höglund, L., Jönsson, B., & Ågren, J. (1990). Computer simulation of multicomponent diffusional transformations in steel. In *Fundamentals and Applications of Ternary Diffusion* (pp. 153–163). Elsevier. <https://doi.org/10.1016/B978-0-08-040412-7.50023-2>
- Andersson, J. O., Helander, T., Höglund, L., Shi, P., & Sundman, B. (2002). Thermo-Calc & DICTRA, computational tools for materials science. *Calphad*, 26(2), 273–312. [https://doi.org/10.1016/S0364-5916\(02\)00037-8](https://doi.org/10.1016/S0364-5916(02)00037-8)
- Apple, C. A., Caron, R. N., & Krauss, G. (1974). Packet microstructure in Fe-0.2 pct C martensite. *Metallurgical Transactions*, 5(3), 593–599.
- Bachmann, F., Hielscher, R., & Schaeben, H. (2010). Texture analysis with MTEX–free and open source software toolbox. In *Solid State Phenomena* (Vol. 160, pp. 63–68). Trans Tech Publications Ltd. <https://doi.org/10.4028/www.scientific.net/ssp.160.63>
- Béranger, G., Henry, G., & Sanz, G. (1996). *The Book of Steel*. Lavoisier Publishing, Intercept LTD.
- Bhadeshia, H., & Honeycombe, R. (2017). *Steels: Microstructure and Properties*. Oxford, United Kingdom: Butterworth-Heinemann Elsevier Ltd.
- Borgenstam, A., Höglund, L., Ågren, J., & Engström, A. (2000). DICTRA, a tool for simulation of diffusional transformations in alloys. *Journal of Phase Equilibria*, 21(3), 269–280. <https://doi.org/10.1361/105497100770340057>
- Bramfitt, B. L., & Benscoter, A. O. (2002). *Metallographer's guide. Practices and Procedures for Irons and Steels*. Materials Park, OH, USA: ASM International, 87(3).
- Bukanin, V., Zenkov, A., & Ivanov, A. (2016). Design of induction heating devices using ELTA and 2DELTA software. In *Proceedings of the 2016 IEEE North West Russia Section Young Researchers in Electrical and Electronic Engineering Conference, EIconRusNW 2016*. <https://doi.org/10.1109/EIconRusNW.2016.7448236>
- Cateau, S. D., Sourmail, T., & Moine, A. (2016). Dilatometric Study of Phase Transformations in Steels: Some Issues. *Materials Performance and Characterization*, 5(5), 20160069. <https://doi.org/10.1520/MPC20160069>
- Celada-Casero, C., Sietsma, J., & Santofimia, M. J. (2019). The role of the austenite grain size in the martensitic transformation in low carbon steels. *Materials and Design*, 167. <https://doi.org/10.1016/j.matdes.2019.107625>
- Chen, Q., Wu, K., Sterner, G., & Mason, P. (2014). Modeling Precipitation Kinetics During Heat Treatment with Calphad-Based Tools. *Journal of Materials Engineering and Performance*, 23(12), 4193–4196. <https://doi.org/10.1007/s11665-014-1255-6>
- Clarke, A. J., Speer, J. G., Miller, M. K., Hackenberg, R. E., Edmonds, D. V., Matlock, D. K., ... De Moor, E. (2008). Carbon partitioning to austenite from martensite or bainite during the quench and partition (Q&P) process: A critical assessment. *Acta Materialia*, 56(1), 16–22. <https://doi.org/10.1016/j.actamat.2007.08.051>

- Das, C. R., Bhaduri, A. K., Srinivasan, G., Shankar, V., & Mathew, S. (2009). Selection of filler wire for and effect of auto tempering on the mechanical properties of dissimilar metal joint between 403 and 304L(N) stainless steels. *Journal of Materials Processing Technology*, 209(3), 1428–1435. <https://doi.org/10.1016/j.jmatprotec.2008.03.053>
- De Moor, E., Speer, J. G., Matlock, D. K., Kwak, J. H., & Lee, S. B. (2011). Effect of carbon and manganese on the quenching and partitioning response of CMnSi steels. *ISIJ International*, 51(1), 137–144. <https://doi.org/10.2355/isijinternational.51.137>
- Durand-Charre, M. (2004). *Microstructure of Steels and Cast Irons*. Berlin Heidelberg, Germany: Springer-Verlag. <https://doi.org/10.1007/978-3-662-08729-9>
- García de Andrés, C. (2002). Application of dilatometric analysis to the study of solid–solid phase transformations in steels. *Materials Characterization*, 48(1), 101–111. [https://doi.org/10.1016/S1044-5803\(02\)00259-0](https://doi.org/10.1016/S1044-5803(02)00259-0)
- Hidalgo, J., & Santofimia, M. J. (2016). Effect of Prior Austenite Grain Size Refinement by Thermal Cycling on the Microstructural Features of As-Quenched Lath Martensite. *Metallurgical and Materials Transactions A*, 47(11), 5288–5301. <https://doi.org/10.1007/s11661-016-3525-4>
- Hillert, M., Höglund, L., & Ågren, J. (1993). Escape of carbon from ferrite plates in austenite. *Acta Metallurgica et Materialia*, 41(7), 1951–1957. [https://doi.org/10.1016/0956-7151\(93\)90365-Y](https://doi.org/10.1016/0956-7151(93)90365-Y)
- Hosford, W. F. (2012). *Iron and Steel*. Cambridge, UK: Cambridge University Press. <https://doi.org/10.1017/CBO9781139086233>
- Hou, Z., Hedström, P., Xu, Y., Di, W., & Odqvist, J. (2014). Microstructure of Martensite in Fe–C–Cr and its Implications for Modelling of Carbide Precipitation during Tempering. *ISIJ International*, 54(11), 2649–2656. <https://doi.org/http://doi.org/10.2355/isijinternational.54.2649>
- Huang, X., Morito, S., Hansen, N., & Maki, T. (2012). Ultrafine structure and high strength in cold-rolled martensite. *Metallurgical and Materials Transactions A: Physical Metallurgy and Materials Science*, 43(10), 3517–3531. <https://doi.org/10.1007/s11661-012-1275-5>
- Hutchinson, B., Hagström, J., Karlsson, O., Lindell, D., Tornberg, M., Lindberg, F., & Thuvander, M. (2011). Microstructures and hardness of as-quenched martensites (0.1–0.5%C). *Acta Materialia*, 59(14), 5845–5858. <https://doi.org/10.1016/j.actamat.2011.05.061>
- Kamyabi-Gol, A., Clark, S. J., Gibbs, J. W., Sridhar, S., & Mendez, P. F. (2016). Quantification of evolution of multiple simultaneous phase transformations using dilation curve analysis (DCA). *Acta Materialia*, 102, 231–240. <https://doi.org/10.1016/j.actamat.2015.09.025>
- Kaufman, L., & Ågren, J. (2014). CALPHAD, first and second generation – Birth of the materials genome. *Scripta Materialia*, 70, 3–6. <https://doi.org/10.1016/j.scriptamat.2012.12.003>
- Kelly, P. M., Jostsons, A., & Blake, R. G. (1990). The orientation relationship between lath martensite and austenite in low carbon, low alloy steels. *Acta Metallurgica et Materialia*, 38(6), 1075–1081. [https://doi.org/10.1016/0956-7151\(90\)90180-O](https://doi.org/10.1016/0956-7151(90)90180-O)

- Klein, S., Mujica Roncery, L., Walter, M., Weber, S., & Theisen, W. (2017). Diffusion processes during cementite precipitation and their impact on electrical and thermal conductivity of a heat-treatable steel. *Journal of Materials Science*, 52(1), 375–390. <https://doi.org/10.1007/s10853-016-0338-1>
- Koistinen, D. P., & Marburger, R. E. (1959). A general equation prescribing the extent of the austenite-martensite transformation in pure iron-carbon alloys and plain carbon steels. *Acta Metallurgica*, 7(1), 59–60. [https://doi.org/10.1016/0001-6160\(59\)90170-1](https://doi.org/10.1016/0001-6160(59)90170-1)
- Kömi, J., Karjalainen, P., & Porter, D. (2016). Direct-Quenched Structural Steels. In *Encyclopedia of Iron, Steel, and Their Alloys*. <https://doi.org/10.1081/e-eisa-120049737>
- Krauss, G. (1990). *Steels: Heat treatment and processing principles*. Materials Park, Ohio: ASM International.
- Krauss, G. (2002). Martensite in steel: strength and structure. *Materials Science and Engineering: A*, 273–275(July), 40–57. [https://doi.org/10.1016/s0921-5093\(99\)00288-9](https://doi.org/10.1016/s0921-5093(99)00288-9)
- Kung, C. Y., & Rayment, J. J. (1982). An examination of the validity of existing empirical formulae for the calculation of ms temperature. *Metallurgical Transactions A*, 13(2), 328–331. <https://doi.org/10.1007/BF02643327>
- Langer, J. S., & Schwartz, A. J. (1980). Kinetics of nucleation in near-critical fluids. *Physical Review A*, 21(3), 948–958. <https://doi.org/10.1103/PhysRevA.21.948>
- Lee, S. J., & Van Tyne, C. J. (2012). A kinetics model for martensite transformation in plain carbon and low-alloyed steels. *Metallurgical and Materials Transactions A: Physical Metallurgy and Materials Science*, 43(2), 422–427. <https://doi.org/10.1007/s11661-011-0872-z>
- Li, C. N., Yuan, G., Ji, F. Q., Ren, D. S., & Wang, G. D. (2016). Effects of auto-tempering on microstructure and mechanical properties in hot rolled plain C-Mn dual phase steels. *Materials Science and Engineering A*, 665, 98–107.
- Lukas, H. L., Fries, S. G., & Sundman, B. (2007). *Computational thermodynamics: The Calphad method*. *Computational Thermodynamics: The Calphad Method*. <https://doi.org/10.1017/CBO9780511804137>
- Matsuda, H., Mizuno, R., Funakawa, Y., Seto, K., Matsuoka, S., & Tanaka, Y. (2013). Effects of auto-tempering behaviour of martensite on mechanical properties of ultra high strength steel sheets. *Journal of Alloys and Compounds*, 577, S661–S667. <https://doi.org/10.1016/j.jallcom.2012.04.108>
- Modaresi, R., Pauliuk, S., Løvik, A. N., & Müller, D. B. (2014). Global Carbon Benefits of Material Substitution in Passenger Cars until 2050 and the Impact on the Steel and Aluminum Industries. *Environmental Science & Technology*, 48(18), 10776–10784. <https://doi.org/10.1021/es502930w>
- Mohrbacher, H. (2018). Property optimization in as-quenched martensitic steel by molybdenum and niobium alloying. *Metals*, 8(4), 234.
- Morito, S., Nishikawa, J., & Maki, T. (2003). Dislocation Density within Lath Martensite in Fe-C and Fe-Ni Alloys. *ISIJ International*, 43(9), 1475–1477. <https://doi.org/10.2355/isijinternational.43.1475>

- Morito, S., Tanaka, H., Konishi, R., Furuhashi, T., & Maki, A. T. (2003). The morphology and crystallography of lath martensite in Fe-C alloys. *Acta materialia*, 51(6), 1789–1799. [https://doi.org/10.1016/S1359-6454\(02\)00577-3](https://doi.org/10.1016/S1359-6454(02)00577-3)
- Morris Jr, J. W., Kinney, C., Pytlewski, K., & Adachi, Y. (2013). Microstructure and cleavage in lath martensitic steels. *Science and Technology of Advanced Materials*, 14(1), 014208. <https://doi.org/10.1088/1468-6996/14/1/014208>
- Morsdorf, L., Jeannin, O., Barbier, D., Mitsuhara, M., Raabe, D., & Tasan, C. C. (2016). Multiple mechanisms of lath martensite plasticity. *Acta Materialia*, 121, 202–214.
- Morsdorf, L., Tasan, C. C., Ponge, D., & Raabe, D. (2015). Acta Materialia 3D structural and atomic-scale analysis of lath martensite: Effect of the transformation sequence. *Acta Materialia*, 95, 366–377. <https://doi.org/10.1016/j.actamat.2015.05.023>
- Morsdorf, L. (2017). *Fundamentals of ferrous low-carbon lath martensite: from the as-quenched, to tempered and deformed states* (Doctoral dissertation, RWTH Aachen Aachen, Germany).
- Nam, J. H., Yu, S. H., & Lee, Y. K. (2019). Effect of auto-tempering on the cold roll-ability of medium-Mn steel. *Materials Science and Technology (United Kingdom)*, 35(17), 2069–2075. <https://doi.org/10.1080/02670836.2018.1547474>
- Nyssonen, T., Peura, P., & Kuokkala, V. T. (2018). Crystallography, Morphology, and Martensite Transformation of Prior Austenite in Intercritically Annealed High-Aluminum Steel. *Metallurgical and Materials Transactions A: Physical Metallurgy and Materials Science*, 49(12), 6426–6441. <https://doi.org/10.1007/s11661-018-4904-9>
- Oliveira, F. L. G., Andrade, M. S., & Cota, A. B. (2007). Kinetics of austenite formation during continuous heating in a low carbon steel. *Materials Characterization*, 58(3), 256–261. <https://doi.org/10.1016/j.matchar.2006.04.027>
- Peng, F., Xu, Y., Han, D., & Gu, X. (2019). Kinetic models of multiple-stage martensite transformation and subsequent isothermal bainite formation excluding  $\epsilon$ -carbide precipitation in intercritical quenching and partitioning steels. *Materials & Design*, 183, 108183. <https://doi.org/10.1016/j.matdes.2019.108183>
- Pereloma, E., & Edmonds, D. V. (Eds.). (2012). Phase transformations in steels: Diffusionless transformations, high strength steels, modelling and advanced analytical techniques. Swanston, UK: Woodhead Publishing.
- Reisinger, S., Ressel, G., Eck, S., & Marsoner, S. (2017). Differentiation of grain orientation with corrosive and colour etching on a granular bainitic steel. *Micron*, 99(March), 67–73. <https://doi.org/10.1016/j.micron.2017.04.002>
- Semiatin, S. L., Mahaffey, D. W., Levkulich, N. C., & Senkov, O. N. (2017). The Radial Temperature Gradient in the Gleeble Hot-Torsion Test and Its Effect on the Interpretation of Plastic-Flow Behavior. *Metallurgical and Materials Transactions A*, 48(11), 5357–5367. <https://doi.org/10.1007/s11661-017-4296-2>
- Sourmail, T., & Smanio, V. (2013). Determination of  $M_s$  temperature: methods, meaning and influence of ‘slow start’ phenomenon. *Materials Science and Technology*, 29(7), 883–888. <https://doi.org/10.1179/1743284713Y.0000000209>

- Speich, G. R. (1969). Tempering of low-carbon martensite. *Transactions of the Metallurgical Society of AIME*, 245(12), 2553–2564.
- Speich, G. R., & Leslie, W. C. (1972). Tempering of steel. *Metallurgical Transactions*, 3(5), 1043–1054. <https://doi.org/10.1007/BF02642436>
- Sperle, J. O., & Hallberg, L. (2011). Environmental advantages of using high strength steel. In *The 2nd International Conference on Clean Technologies in the Steel Industry, Budapest*.
- Sundman, B., Jansson, B., & Andersson, J.-O. (1985). The Thermo-Calc databank system. *Calphad*, 9(2), 153–190. [https://doi.org/10.1016/0364-5916\(85\)90021-5](https://doi.org/10.1016/0364-5916(85)90021-5)
- Takaki, S., Akama, D., & Tsuchiyama, T. (2017). Quantitative Evaluation of Auto-Tempering During Quenching. *NETSUSHORI*, 56(6), 340–344.
- Thermo-Calc Software AB. (2019). *Precipitation Module (TC-PRISMA) User Guide: Thermo-Calc Version 2019b*. Retrieved from <https://thermocalc.com/content/uploads/Documentation/Archive/2015-2019/2019b/2019b-precipitation-module-tc-prisma-user-guide.pdf>
- Thomas, G. A., Danoix, F., Speer, J. G., Thompson, S. W., & Cuvelly, F. (2014). Carbon atom re-distribution during quenching and partitioning. *ISIJ international*, 54(12), 2900–2906.
- van Bohemen, S. M. C. (2013). The nonlinear lattice expansion of iron alloys in the range 100–1600K. *Scripta Materialia*, 69(4), 315–318.
- van Bohemen, S. M. C., & Sietsma, J. (2009). Martensite formation in partially and fully austenitic plain carbon steels. *Metallurgical and Materials Transactions A*, 40(5), 1059–1068. <https://doi.org/10.1179/174328408X365838>
- Villa, M., & Somers, M. A. J. (2020). On the Role of Isothermal Martensite Formation during Cryogenic Treatment of Steels. *HTM Journal of Heat Treatment and Materials*, 75(5), 263–286. <https://doi.org/10.3139/105.110420>
- Windisch, E., Benezech, V., Chen, G., & Kauppila, J. (2017). *Lightening Up: How Less Heavy Vehicles Can Help Cut CO<sub>2</sub> Emissions*. Paris, France: International Transport Forums. Retrieved from <https://www.itf-oecd.org/sites/default/files/docs/less-heavy-vehicles-cut-co2-emissions.pdf>
- Wagner, R., Kampmann, R., & Voorhees, P. W. (2005). Homogeneous Second-Phase Precipitation. In *Phase Transformations in Materials*. Weinheim, Germany: Wiley-VCH Verlag GmbH & Co. <https://doi.org/10.1002/352760264x.ch5>
- Wang, J., Wolk, P. J. van der, & Zwaag, S. van der. (2000). Determination of Martensite Start Temperature in Engineering Steels Part I. Empirical Relations Describing the Effect of Steel Chemistry. *Materials Transactions, JIM*, 41(7), 761–768. <https://doi.org/10.2320/matertrans1989.41.761>
- Wert, C. A. (1950). Diffusion Coefficient of C in alpha-Iron. *Physical Review*, 79(4), 601–605. <https://doi.org/10.1103/PhysRev.79.601>
- Yamashita, T., Tanaka, Y., Nagoshi, M., & Ishida, K. (2016). Novel technique to suppress hydrocarbon contamination for high accuracy determination of carbon content in steel by FE-EPMA. *Scientific Reports*, 6(1), 29825. <https://doi.org/10.1038/srep29825>

- Yang, H. S., & Bhadeshia, H. K. D. H. (2009). Austenite grain size and the martensite-start temperature. *Scripta Materialia*, 60(7), 493–495.
- Yang, H. S., & Bhadeshia, H. K. D. H. (2007). Uncertainties in dilatometric determination of martensite start temperature. *Materials Science and Technology*, 23(5), 556-560. <https://doi.org/10.1179/174328407X176857>
- Zener, C. (1946). Kinetics of the decomposition of austenite. *Transactions of the Metallurgical Society of AIME*, 167, 550–595.
- Zhao, J. Z., Mesplont, C., & De Cooman, B. C. (2002). Quantitative analysis of the dilatation during an isothermal decomposition of austenites. *Materials Science and Engineering: A*, 332(1–2), 110–116. [https://doi.org/10.1016/S0921-5093\(01\)01723-3](https://doi.org/10.1016/S0921-5093(01)01723-3)

## Original publications

- I Ramesh Babu, S., Ivanov, D., & Porter, D. (2019). Influence of microsegregation on the onset of the martensitic transformation. *ISIJ International*, 59(1), 169–175.
- II Ramesh Babu, S., Jaskari, M., Järvenpää, A., & Porter, D. (2019). The effect of hot-mounting on the microstructure of an as-quenched auto-tempered low-carbon martensitic steel. *Metals*, 9(5), 550.
- III Ramesh Babu, S., Nyysönen, T., Jaskari, M., Järvenpää, A., Davis, T. P., Pallaspuro, S., Kömi, J., & Porter, D. (2019). Observations on the relationship between crystal orientation and the level of auto-tempering in an as-quenched martensitic steel. *Metals*, 9(12), 1255.
- IV Ramesh Babu, S., Davis, T. P., Haas, T., Jarvenpää, A., Kömi, J., & Porter, D. (2020). Image processing tool quantifying auto-tempered carbides in as-quenched low carbon martensitic steels. *Metals*, 10(2), 171.
- V Ramesh Babu, S., Jaskari, M., Jarvenpää, A., Davis, T. P., Kömi, J., & Porter, D. (2020). Precipitation versus partitioning kinetics during the quenching of low-carbon martensitic steels. *Metals*, 10(7), 850.

Reprinted with permission from The Iron and Steel Institute of Japan [ISIJ] (Paper I © 2019 ISIJ) and under CC-BY 4.0 license (Papers II–V © 2019, 2020 Authors).

Original publications are not included in the electronic version of the dissertation.



759. Alasalmi, Tuomo (2020) Uncertainty of classification on limited data
760. Kinnunen, Hannu (2020) Studies for the development, validation, and application of wearable technology in the assessment of human health-related behavior
761. Abou Zaki, Nizar (2020) The role of agriculture expansion in water resources depletion in central Iran
762. Gyakwaa, Francis (2020) Application of Raman spectroscopy for the characterisation of synthetic non-metallic inclusions found in Al-killed calcium treated steels
763. Pandya, Abhinay (2020) Demographic inference and affect estimation of microbloggers
764. Eckhardt, Jenni (2020) Mobility as a Service for public-private partnership networks in the rural context
765. Apilo, Olli (2020) Energy efficiency analysis and improvements of MIMO cellular communications
766. Gogoi, Harshita (2020) Development of biosorbents for treatment of industrial effluents and urban runoffs
767. Saavalainen, Paula (2020) Sustainability assessment tool for the design of new chemical processes
768. Ferdinando, Hany (2020) Classification of ultra-short-term ECG samples : studies on events containing violence
769. Leinonen, Marko (2020) Over-the-air measurements, tolerances and multiradio interoperability on 5G mmW radio platform
770. Pakkala, Daniel (2020) On design and architecture of person-centric digital service provisioning : approach, fundamental concepts, principles and prototypes
771. Mustaniemi, Janne (2020) Computer vision methods for mobile imaging and 3D reconstruction
772. Khan, Uzair Akbar (2020) Challenges in using natural peatlands for treatment of mining-influenced water in a cold climate : considerations for arsenic, antimony, nickel, nitrogen, and sulfate removal
773. Kumar, Tanesh (2020) Secure edge services for future smart environments
774. Laitila, Juhani Markus (2021) Effect of forced weld cooling on high-strength low alloy steels to interpass temperature

S E R I E S E D I T O R S

**A**  
**SCIENTIAE RERUM NATURALIUM**  
*University Lecturer Tuomo Glumoff*

**B**  
**HUMANIORA**  
*University Lecturer Santeri Palviainen*

**C**  
**TECHNICA**  
*Postdoctoral researcher Jani Peräntie*

**D**  
**MEDICA**  
*University Lecturer Anne Tuomisto*

**E**  
**SCIENTIAE RERUM SOCIALIUM**  
*University Lecturer Veli-Matti Ulvinen*

**E**  
**SCRIPTA ACADEMICA**  
*Planning Director Pertti Tikkanen*

**G**  
**OECONOMICA**  
*Professor Jari Juga*

**H**  
**ARCHITECTONICA**  
*University Lecturer Anu Soikkeli*

**EDITOR IN CHIEF**  
*University Lecturer Santeri Palviainen*

**PUBLICATIONS EDITOR**  
*Publications Editor Kirsti Nurkkala*

ISBN 978-952-62-2833-4 (Paperback)  
ISBN 978-952-62-2834-1 (PDF)  
ISSN 0355-3213 (Print)  
ISSN 1796-2226 (Online)